Numerical simulation of extensional deformations of viscoelastic liquid bridges in filament stretching devices

Minwu Yao [a],*, Gareth H. McKinley [b]

[a] *Ohio Aerospace Institute, 22800 Cedar Point Road, Brook Park, OH 44142, USA*
[b] *Division of Applied Sciences, Harvard University, Cambridge, MA 02138, USA*

Abstract

Large extensional deformations of viscoelastic fluid columns in filament stretching rheometers are studied through numerical simulations up to Hencky strains of greater than $\varepsilon = 4$. The time-dependent axisymmetric calculations incorporate the effects of viscoelasticity, surface tension, fluid inertia, plus a deformable free surface and provide quantitative descriptions of the evolution in the filament profile, the kinematics in the liquid column and the resulting dynamic evolution in the viscous and elastic contributions to the total stress. In addition to investigating the variation in the apparent Trouton ratio expected in experimental measurements using this new type of extensional rheometer, we also investigate the generic differences between the response of Newtonian and viscoelastic fluid filaments described by the Oldroyd-B model. For small strains, the fluid deformation is governed by the Newtonian solvent contribution to the stress and the filament evolution is very similar in both the Newtonian and viscoelastic cases. However, in the latter case at large strains and moderate Deborah numbers, elastic stresses dominate leading to strain-hardening in the axial mid-regions of the column and subsequent drainage of the quasi-static liquid reservoir that forms near both end-plates. These observations are in good qualitative agreement with experimental observations. For small initial aspect ratios and low strains, the non-homogeneous deformation predicted by numerical simulations is well described by a lubrication theory solution. At larger strains, the initial flow non-homogeneity leads to the growth of viscoelastic stress boundary layers near the free surface which can significantly affect the transient Trouton ratio measured in the device. Exploratory design calculations suggest that mechanical methods for modifying the boundary conditions at the rigid end-plates can reduce this non-homogeneity and lead to almost ideal uniaxial elongational flow kinematics. © 1998 Elsevier Science B.V.

Keywords: Extensional flow; Fluid dynamics; Finite element method; Liquid bridge; Filament stretching device; Viscoelasticity; Oldroyd-B fluid; Moving boundary problem

* Corresponding author. Tel.: + 1 216 9623094; fax: + 1 216 9623120.

1. Introduction

The key to a better understanding of the extensional behavior of polymer liquids in complex flows is the accurate, unambiguous quantitative measurement of extensional rheological material properties [1]. Filament stretching devices are one of the most promising techniques that have been developed for providing accurate measurements of transient elongational stress growth functions for viscous polymer solutions [2]. Such filament stretching devices are currently being developed by several independent research groups around the world and in the present paper we refer extensively to the work of Sridhar and Tirtaatmadja [3,4], Kröger, Berg et al. [5,6], Solomon and Muller [7], and McKinley and Spiegelberg et al. [8–10]. In the filament stretching apparatus, a cylindrical liquid column is first generated between two concentric circular plates and then is elongated by pulling one or both of the end-plate fixtures at an exponentially increasing rate. It is hoped that the resulting flow kinematics in the liquid column approximate an ideal uniaxial elongational flow, and the extensional viscosity is determined from the axial force at the end-plate which is measured as a function of time [11].

The major problems with the conventional filament stretching configuration are: (i) the presence of a deformable free surface and (ii) the two rigid, non-deforming end-plates. The former leads to a significant 'necking' in the central region of liquid bridge due to the surface tension of the fluid and the latter results in an appreciable shear component in the deformation history due to the no-slip boundary condition at the rigid end-plates. As a result the elongation is not shear-free, the extension rate is spatially and temporally inhomogeneous and analysis of the experimental results does not lead to true extensional material properties, but an 'apparent extensional viscosity' [2].

To overcome the experimental difficulties, two approaches that modify the fluid kinematics in such devices have been proposed in the literature. One is the velocity compensation algorithm which was first successfully used by Tirtaatmadja and Sridhar [4] and more recently by Spiegelberg et al. [9]. In this approach the imposed velocity at the moving plate is modified in such a way that a constant 'effective' extension rate, defined on the basis of the measured radius and velocity at the mid-plane of the filament, can be achieved at the axial mid-section of the filament. This strategy provides more accurate extensional rheological measurements despite the fact that the extension rate in the liquid column remains spatially inhomogeneous along the axial direction as we show below in our numerical results. The second approach focuses on generating homogeneous uniaxial elongational kinematics by simultaneously elongating the sample axially and reducing the diameter of the end-plate fixtures at an exponential rate. Since the imposed axial and radial velocity components at the two end-plates provide the boundary conditions necessary for homogeneous uniaxial elongational flow, this approach in theory leads to a perfect cylindrical fluid column and a constant extensional strain rate both in space and throughout the duration of the test. At large strains, the cylindrical fluid column rapidly exceeds the static stability criterion of Rayleigh $L \geq 2\pi R$ [8]; however, as we show below, capillary break-up is greatly retarded as a result of the high viscosity of the fluid column. This latter approach will be referred to as a reducing diameter device (RDD) herewith. Experiments with a RDD were first carried out by Berg et al. [6] under microgravity conditions. One inherent limit with such a RDD is that the radial engineering strain (defined by the ratio of ultimate diameter over the initial diameter) that can be achieved is usually restricted by the mechanical design of

the instrument to be much lower than the total axial strain of the experiment. In the experiments of Berg et al., a final reduction ratio of two was achieved (namely the end-plate diameter was reduced by half at the end of experiments). In the present work, we investigate the consequences of such limitations and explore possible enhancement in the accuracy of the measured material properties that may be achieved by increasing the final reduction ratio of a mechanical RDD.

Despite the rapid proliferation of filament stretching rheometers, there are few theoretical studies of these devices. Broad qualitative agreement between experimental measurements of a single fluid in different laboratories has been demonstrated [4,9], and the measurements have been fitted with single and multi-mode formulations of viscoelastic constitutive models [12]. However, observations have shown that the geometric configuration of the device can affect the fluid kinematics and the dynamical evolution in the tensile force [9] and also lead to the onset of elastic flow instabilities [10]. Large discrepancies between the measured material functions at large strains and the asymptotic steady state value estimated from molecular considerations have also been noted [13]. Before new constitutive models are sought, however, it is necessary to verify through numerical calculation that the device is behaving as expected. Similar calculations for other extensional flow devices, such as opposed jet rheometers have revealed that large deviations from the expected kinematics can exist even for Newtonian fluids [14,15]. Such simulations can also be used to guide the design of future versions of the device.

In this work, we study the dynamic response of axisymmetric viscoelastic liquid bridges in a filament stretching device. As a moving boundary problem, the analysis of the liquid bridge requires three key elements: deformable free surface capabilities, a robust transient algorithm and appropriate constitutive models. Dynamic analysis of the transient free-boundary motion of a non-Newtonian material is computationally challenging. In the literature, relatively little work, either theoretical or numerical, has been reported so far even for the case of Newtonian fluids. Analytical solutions are available only under certain restrictive presumptions, and numerical solutions have been limited to small total deformations. In an early numerical study [16], Shipman et al. simulated one of the low-rate falling-plate extensional rheometer experiments conducted by Sridhar and co-workers using a free-surface finite element method and the Oldroyd-B constitutive model. A reasonable agreement in free surface shapes with the experiment was obtained. However, computational restrictions introduced several ambiguities in their model. First, the finite element mesh was constrained to a fixed axial length and consequently only a part of the deforming domain was modeled. Second, at the truncated boundary, the theoretical steady-state extensional stress was used to approximate the unknown stress boundary condition. The third ambiguity was introduced by neglecting the effects of fluid outside the fixed control volume. Finally, the simulation was not started at $t = 0$, but at $t = 2.42$ s, while equilibrium initial conditions for the polymeric stress were used and hence any effects of the initial configuration of the device were not captured. In another numerical investigation [8], Gaudet et al. used the boundary element method to perform a dynamic analysis of Newtonian liquid bridges for a wide range of aspect ratios and capillary numbers. In their work, the fluid motion was assumed to be quasi-steady by neglecting the inertia terms in the momentum equation and the fluid motion was governed by the linear Stokes equations. The viscous force exerted by the fluid on the stationary end-plate was computed as a function of strain; however, in this study the end-plates were separated linearly in time rather than in the exponential manner employed in filament stretching rheometers. In a more recent work [29], Sizaire and Legat

studied the extensional response of the Boger fluid in the filament stretching devices using an approximate version of the finitely extensible non-linear elastic dumbbell model modified by Chilcott and Rallison (FENE-CR). The inertia and gravity effects were neglected in their free-surface finite element solutions for the viscoelastic moving boundary problem and the results were compared with the experimental measurements by Spiegelberg and McKinley. Good qualitative agreement with the experiments was found, however, the spatial and temporal inhomogeneity of the kinematics generated by the device were not investigated in detail.

The present study is based on an axi-symmetric model of the liquid bridge which incorporates the viscoelastic behavior of the liquid, surface tension, fluid inertia, a deformable free surface and imposed extensional deformations. The primary goals of the present work are: to study the complex time-dependent extensional deformations in filament stretching devices, to compare and contrast differing fluid response for viscoelastic and Newtonian liquid samples, to investigate the effects of initial geometric configuration of the filament, to examine the benefits of adaptive diameter end-plates in minimizing non-homogeneous kinematics within fluid column, and to provide a numerical tool to aid in optimization of experimental designs.

2. Mathematical model

2.1. Description of the problem

We consider the extensional flow of a viscoelastic liquid contained between two parallel coaxial massless circular disks. The liquid column and the rigid end-plates represent the basic elements that comprise a filament stretching apparatus and are usually referred to in combination as a liquid bridge [8]. In order to match the experimental configuration, the lower plate is held fixed at all times in the calculations as shown in Fig. 1(a) and, hence, will be referred to as the fixed end-plate. In the absence of inertia (of the fluid or of the end-plates) the equations of motion are Galilean-invariant and our computed results are unchanged if both plates are separated exponentially in time.
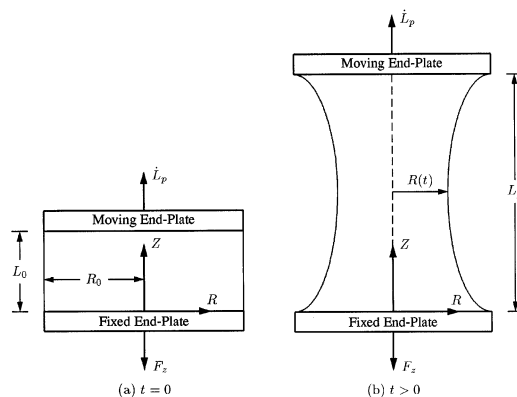

Fig. 1. (a) Initial configuration of the cylindrical liquid bridge. (b) Subsequent extensional deformation of the liquid bridge.

The initial configuration of the liquid bridge is a cylinder when $t \leq 0^-$. Let R_0 denote the radius of the two equal end-plates and L_0 the initial separation between the two end-plates. The initial aspect ratio of the liquid bridge is then defined as

$$\Lambda_0 \equiv L_0/R_0. \tag{1}$$

At the instant $t = 0^+$, the top plate is set into motion which results in a transient extensional deformation of the liquid column as depicted schematically in Fig. 1(b). The fluid column is assumed to remain axisymmetric and to wet the end-plate at all times. The contact line is thus pinned to the radial edges of the disks. This agrees with experimental observations of the fluid configuration near the end-plates, except at very high tensile stresses and large strains [10]. During the deformation, the dynamic length of the liquid bridge is denoted by $L_p(t)$ and the transient aspect ratio

$$\Lambda_t \equiv L_p(t)/R_0 \tag{2}$$

increases with time while the volume of the liquid bridge remains constant. The top plate will be referred to as the moving end-plate and its axial velocity is $\dot{L}_p = dL_p/dt$. In this study, we are particularly interested in the exponential separation between the two end-plates which is prescribed by

$$L_p(t) = L_0 e^{\dot{\varepsilon}_0 t} \quad \text{and} \quad \dot{L}_p(t) = L_0 \dot{\varepsilon}_0 e^{\dot{\varepsilon}_0 t}, \tag{3}$$

where $\dot{\varepsilon}_0$ is the imposed constant extension rate, and $(L_0 \dot{\varepsilon}_0) \equiv V_0$ is the initial velocity of the moving end-plate.

2.2. Governing equations

The fluid flow within the liquid bridge is assumed to be isothermal, incompressible and axi-symmetric and is governed by the incompressibility condition and the equations of motion:

$$\nabla \cdot \boldsymbol{u} = 0, \tag{4}$$

$$\rho \left(\frac{\partial \boldsymbol{u}}{\partial t} + \boldsymbol{u} \cdot \nabla \boldsymbol{u} \right) = \nabla \cdot \boldsymbol{T} + \boldsymbol{F}. \tag{5}$$

Here ρ is the density, $\boldsymbol{u}$ is the velocity vector, $\boldsymbol{F}$ is the body force and $\boldsymbol{T}$ is the Cauchy stress tensor

$$\boldsymbol{T} \equiv -p\boldsymbol{I} + \tau, \tag{6}$$

where p is an isotropic pressure, $\boldsymbol{I}$ is the unit tensor and τ is the extra stress tensor. In this work, we consider the simplest generally admissible differential constitutive model for polymer solutions, the convected Jeffreys model [11] or Oldroyd-B model [17]. In this model, the solvent contribution τ_s and the polymeric contribution τ_p to the extra stress are defined as

$$\tau = \tau_s + \tau_p, \tag{7}$$

$$\tau_s = 2\eta_s \boldsymbol{D}, \tag{8}$$

$$\tau_{\mathrm{p}} + \lambda_1 \left[\frac{\partial \tau_{\mathrm{p}}}{\partial t} + \boldsymbol{u} \cdot \nabla \tau_{\mathrm{p}} - (\nabla \boldsymbol{u})^{\mathrm{T}} \cdot \tau_{\mathrm{p}} - \tau_{\mathrm{p}} \cdot (\nabla \boldsymbol{u}) \right] = 2 \eta_{\mathrm{p}} \boldsymbol{D}, \tag{9}$$

where the rate-of-strain tensor is defined as

$$\boldsymbol{D} \equiv \tfrac{1}{2} [\nabla \boldsymbol{u} + (\nabla \boldsymbol{u})^{\mathrm{T}}], \tag{10}$$

and the three physical parameters involved in this model are the solvent viscosity η_{s}, the polymer contribution to the viscosity η_{p} and the fluid relaxation time λ_1.

At large strains, experiments [4,9] suggest that finite extensibility of the macromolecules may lead to an asymptotic or steady state value in the extensional stresses. Such effects can be captured numerically by incorporating a finitely extensible nonlinear elastic (FENE) spring into the kinetic theory leading to Eqs. (7)–(9). However for realistic values of $L \sim 50$ (L represents the ratio of the length of a fully extended dumbbell to its equilibrium length), the FENE nonlinearity does not affect the evolution of the filament until large strains $\varepsilon > 4$ [9]. Since we are primarily interested in a general understanding the basic differences between Newtonian and viscoelastic fluid samples, we therefore do not consider finite extensibility in the present work.

The complete boundary conditions for this problem include: the no-slip condition along the interface between the liquid and the end-plates, axi-symmetric along the z-axis, the prescribed motion given by Eq. (3) at the moving end-plate, and the following kinematic and dynamic conditions

$$\frac{\partial S}{\partial t} + \boldsymbol{u} \cdot \nabla S = 0, \tag{11}$$

$$\boldsymbol{T} \cdot \boldsymbol{n} = (2 \sigma H - p_{\mathrm{a}}) \boldsymbol{n}, \tag{12}$$

on the deformable free surface boundary. Here $S(r, z, t) \equiv [R(z, t) - r] = 0$ is a function that defines the spatial position of the free surface $R(z, t)$, $\boldsymbol{n}$ is the unit norm of the surface, p_{a} is the ambient pressure, H is the mean Gaussian curvature of the free surface and σ is the surface tension coefficient. In addition, the following initial conditions for the velocity, pressure and extra stress fields:

$$\boldsymbol{u}(r, z) = 0, \qquad p(r, z) - p_{\mathrm{a}} = 0 \quad \text{and} \quad \tau(r, z) = 0 \quad \text{at } t \leq 0^-, \tag{13}$$

also need to be imposed. Eqs. (4)–(13) plus the boundary conditions form a well-posed set of governing equations for the moving boundary problem of viscoelastic liquid bridges.

2.3. Dimensionless scaling

We choose to scale lengths and time with the initial radius R_0 and the imposed stretch rate $1/\dot{\varepsilon}_0$, respectively. Stresses and pressures are scaled with $\eta_0 \dot{\varepsilon}_0$ where $\eta_0 = \eta_{\mathrm{s}} + \eta_{\mathrm{p}}$ is the total viscosity of the fluid and velocities are nondimensionalized with the product $\dot{\varepsilon}_0 R_0$. In addition to the geometric aspect ratio Λ_0 defined in Eq. (1) and the Hencky strain $\varepsilon = \dot{\varepsilon}_0 t$ imposed on the filament, the following dimensionless groups are also important in governing the relative magnitude of each force affecting the evolution of the liquid bridge:

The Deborah number

$$\mathrm{De} \equiv \lambda_1 \dot{\varepsilon}_0, \tag{14}$$

Table 1

Geometric parameters and material properties of a polyisobutylene-based Boger fluid (PIB 0.31 wt.%) and a polystyrene-based Boger fluid (PS 0.05 wt.%) used in the calculation

Parameter	Symbol (Unit)	PIB	PS
Plate radius	R_0 (m)	0.0191	0.0170
Initial aspect ratio	Λ_0 (—)	1/3	0.353
Extension rate	$\dot{\varepsilon}_0$ (s^{-1})	2.0	1.03
Density	ρ (kg m^{-3})	894	1026
Solvent viscosity	η_s (Pa·s)	43.2	32.5
Polymer viscosity	η_p (Pa·s)	4.0	5.5
Relaxation time	λ_1 (s)	2.54	3.84
Surface tension coef.	σ (N m^{-1})	0.0285	0.030
Reynolds number	Re $= \rho \dot{\varepsilon}_0 R_0^2 / \eta_0$	0.0138	0.008
Capillary number	Ca $= \eta_0 \dot{\varepsilon}_0 R_0 / \sigma$	63.26	22.18
Bond number	Bo $= \rho g R_0^2 / \sigma$	~ 0	~ 0
Deborah number	De $= \lambda_1 \dot{\varepsilon}_0$	5.08	3.96

the Capillary number

$$\mathrm{Ca} \equiv \eta_0 \dot{\varepsilon}_0 R_0 / \sigma, \tag{15}$$

and the Reynolds number

$$\mathrm{Re} \equiv \rho \dot{\varepsilon}_0 R_0^2 / \eta_0. \tag{16}$$

For the viscous polymer solution, inertial effects are expected to be negligible although the inertia terms of the momentum equation are included in our transient calculations.

In experiments using a given viscoelastic fluid with constant material properties ($\rho, \eta_0, \lambda_1, \sigma$), the ratios

$$\mathrm{De/Re} = \lambda_1 \eta_0 / (\rho R_0^2) \quad \text{and} \quad \mathrm{De/Ca} = \lambda_1 \sigma / (\eta_0 R_0)$$

are constant for all imposed stretch rates $\dot{\varepsilon}_0$. For the purpose of computation we choose to use the material properties for a 0.31 wt.% polyisobutylene Boger fluid (PIB) and a 0.05 wt.% polystyrene Boger fluid (PS) characterized by Spiegelberg et al. [9,10]. The material properties and the values of the dimensionless groups are tabulated in Table 1.

Gravitational body forces on a static liquid bridge are typically characterized by the Bond number [18]

$$\mathrm{Bo} \equiv \rho g R_0^2 / \sigma. \tag{17}$$

In a dynamic simulation of the form considered in the present work, the relative magnitude of the gravitational body force with respect to viscous stresses is given by

$$\mathrm{Bo/Ca} = \rho g R_0 / \eta_0 \dot{\varepsilon}_0. \tag{18}$$

For the small radii of the geometries and high viscosities of the test fluids typically used in experiments, we expect $\mathrm{Bo/Ca} \ll 1$ and we do not include gravitational body forces in the calculations presented here. A study of the effects of an axial gravitational body force via full scale numerical simulation will be presented in a later article [19].

2.4. Calculation of Trouton ratio

One of the primary goals of the filament stretching experiment is to measure the extensional viscosity as a function of Hencky stain. For the ideal uniaxial elongational flow, the extensional viscosity is defined as

$$\eta_E(\dot{\varepsilon}_0, t) \equiv (\tau_{zz} - \tau_{rr})/\dot{\varepsilon}_0, \tag{19}$$

where τ_{zz}, τ_{rr} are the normal components of the extra stress defined in Eq. (7). The Hencky strain ε used in this paper is determined from the displacement of the moving end-plate. For the exponential separation rate, we have

$$\varepsilon \equiv \dot{\varepsilon}_0 t = \ln(L_p/L_0). \tag{20}$$

Calculations of the extensional viscosity, or equivalently the transient Trouton ratio, are usually based on the measured axial force at the end-plate, F_z. The fundamental theoretical results based on the homogeneous stresses in the uniaxial elongational flow are given by

$$T_{zz} + p_0 = \tau_{zz} - \tau_{rr} = \eta_E \dot{\varepsilon}_0, \tag{21}$$

where p_0 is the ambient pressure. For a cylindrical fluid filament with a uniform radius R, the following relationship can be obtained by integrating Eq. (21) over the circular area of the end surface of the liquid column

$$\eta_E = \frac{F_z}{\pi R^2 \dot{\varepsilon}_0}, \tag{22}$$

which relates η_E directly to F_z. In our calculations, the normal force is obtained by the following integral

$$F_z(t) = \int_A [T_{zz}(r, z = 0, t) + p_0] \, dA = F_p + F_v + F_e, \tag{23}$$

where A is the circular domain of the end-plate; F_p, F_v and F_e are pressure, viscous and polymer (elastic) contributions to the normal force, respectively.

The original derivation of Eq. (21) involves the following assumptions [11]: (1) incompressible Newtonian fluid; (2) ideal uniaxial elongational flow with homogeneous extension rate and extra stress; (3) steady state with negligible inertia efffects, i.e. $\partial u/\partial t = 0$ and $u \cdot \nabla u = 0$; (4) no external forces. In practice, the basic relationship Eq. (22) has been generalized to the following form [4,8,9]

$$\text{Tr} \equiv \frac{\eta_E}{\eta_0} = \frac{F_z}{\eta_0 \dot{\varepsilon}_0 \pi R_{\text{mid}}^2} - \frac{\sigma}{\eta_0 \dot{\varepsilon}_0 R_{\text{mid}}} + O(F_i, F_g), \tag{24}$$

where R_{mid} denotes the radius of the fluid filament at the axial mid-plane $z = L_p(t)/2$ and the second term in the right hand side is the surface tension correction term. The final term $O(F_i, F_g)$ accounts for the corrections due to the inertia force F_i and gravitational force F_g, respectively. In the results presented in this paper, this last term is assumed to be negligibly small. Detailed studies of the inertia and gravity corrections will be pursued in later publications. Note that the use of R_{mid} in Eq. (24) implies that the calculated Tr pertains specially to the mid-plane for

non-homogeneous flow situations. In the ideal uniaxial elongational flow of a Newtonian fluid, the Trouton ratio is known to be simply a constant of Tr = 3.

3. Numerical simulation

3.1. Finite element method

Two finite element domains are considered in this study. The first model uses a computational domain bounded by $0 \leq r \leq R(z, t)$ and $0 \leq z \leq L_p(t)$. Since this model considers the whole length of the liquid bridge, it will be referred to as the whole-length model. The second model further assumes symmetry with respect to the mid-plane between the two end-plates. Consequently, the computational domain is defined by $0 \leq r \leq R(z, t)$ and $0 \leq z \leq L_p(t)/2$ and we refer to this configuration as the half-length model. Since the convective inertia forces arising from the $\boldsymbol{u} \cdot \nabla \boldsymbol{u}$ term are, in general, not symmetric, the half-length model is only valid for small Reynolds numbers and small strains.

3.2. Numerical solution

The governing equations are solved using the code POLYFLOW, a commercial finite element method (FEM) program primarily designed for the analysis of flow problems dominated by non-linear viscous phenomena and viscoelastic effects. The details of the FEM formulation and numerical techniques used in POLYFLOW are documented in [20]. Galerkin's method is adopted in the FEM discretization for the momentum equations, and the axi-symmetric FEM mesh is built with the 9-node quadratic quadrilateral element, in which velocity and extra stress are approximated by quadratic shape functions. The pressure is approximated as piecewise linear (i.e. discontinuous on inter-element boundaries). The coordinates of the free surface boundary are interpolated by piecewise linear functions. The transient problem is solved by a predictor–corrector time integration scheme in which the backward Euler method is selected for the corrector. At each time step, the non-linear algebraic system resulting from the FEM discretization is solved by the Newton–Raphson iteration scheme. The non-linear iteration termination is controlled by a specified iteration convergence tolerance of 10^{-5} for the relative error norms of residuals of the governing equations and free surface update.

Another important aspect for moving boundary problems is the remeshing technique which controls mesh deformation by relocating internal nodes according to the displacement of boundary nodes in order to avoid unacceptable element distortions. The Thompson transformation remeshing rule [21] is used in this work. Based on the resolution of a partial differential equation of the elliptic type, the Thompson remeshing technique remains robust even for very large mesh deformations.

3.3. Benchmark test

As a moving boundary problem, the dynamic analysis of liquid bridges is difficult, because the spatial position of the free surface, on which the kinematic and dynamic boundary conditions

are to be applied, is usually unknown a priori and must be solved for as a part of the solution. Consequently, there is, in general, no closed-form (analytical) solution available. Due to the lack of available numerical results to compare our simulations with, it is necessary to conduct benchmark tests in order to check the accuracy of the numerical solutions.

One of the tests considered in this work is the dynamic elongation of a filament with reducing diameter devices (RDD) at both end-plates. In this test, we consider a liquid bridge of a PIB Boger fluid with an initial cylindrical configuration schematically shown in Fig. 1(a). The initial values of velocity, pressure and extra stress are assumed to be zero. The geometry and the material parameters of the PIB Boger fluid are tabulated in Table 1. At $t = 0^+$, the liquid bridge is elongated from the moving end-plate by imposing the exponential velocity profile given in Eq. (3) while the other end-plate is held stationary. In addition, the radius of both end-plates is reduced simultaneously by specifying the following radial velocity condition: $u_r = -0.5\dot{\varepsilon}_0 r$ at the two end-plates. The free surface is still treated as a moving boundary and its position in space is solved as a direct unknown along with other field variables. Since the imposed axial and radial velocities at the two end-plates correspond to the boundary conditions of an ideal uniaxial elongational flow, the test results in a perfect cylindrical free surface and homogeneous extensional deformation history throughout the duration of the simulation. This model test problem is also equivalent to solving the transient start-up of ideal uniaxial elongational flow via a Lagrangian approach. For the Oldroyd-B fluid, the analytical solution is available [11] and hence can be used for validation purposes.

Numerical solutions were obtained using POLYFLOW with 40 quadratic elements. Although the implicit backward time integration scheme was used, a small time-step size corresponding to $\Delta\varepsilon = \dot{\varepsilon}_0 \Delta t = 0.002$ was found to be necessary in order to ensure that the relative errors of the axial deformation of the moving end-plate and radial deformation of the free surface remained less than 1%. The extensional deformations at several typical strain levels are shown in Fig. 2. The free surface does not deflect in this special case. Nevertheless, due to the exponentially increasing velocity of the upper plate, the liquid bridge experiences large extensional deformation in both axial and radial directions. The axial deformation ratio reaches $L_p/L_0 \approx 148$ at a strain level of 5. Since high Hencky strain levels $\varepsilon \geq 5$ need to be attained experimentally to investigate the extensional rheological behavior of polymer liquids, the results shown in Fig. 2 also illustrate one of the great challenges in the liquid bridge modeling, namely the remeshing capabilities for large extensional deformations. To check how the numerical solution quantitatively agrees with the available analytical solution, we present comparison plots of the radial deformation of the free surface versus Hencky strain in Fig. 3(a) and the computed Trouton ratio in Fig. 3(b), respectively. As can be seen from Fig. 3, the agreement between theory and the calculation is excellent and the Trouton ratio is initially $\mathrm{Tr}(0^+) = 3\eta_s/\eta_0 = 2.75$ and subsequently increases exponentially without bound as expected theoretically. The curve denoted by 'Theory' in Fig. 3 is based on the following analytical solution [11]:

$$\eta_E = 3\eta_s + \frac{2\eta_p}{1 - 2\lambda_1\dot{\varepsilon}_0}[1 - e^{-(1 - 2\lambda_1\dot{\varepsilon}_0)t/\lambda_1}] + \frac{\eta_p}{1 + \lambda_1\dot{\varepsilon}_0}[1 - e^{-(1 + \lambda_1\dot{\varepsilon}_0)t/\lambda_1}], \tag{25}$$

for the start-up uniaxial elongational flow with an imposed extension rate $\dot{\varepsilon}_0$.

4. Conventional filament stretching devices

In this section we study the conventional design of filament stretching devices in which the two circular end-plates have an equal and fixed diameter throughout the stretching process. The extensional deformation of the liquid bridge is investigated in increasing levels of details through the global evolution of the free surface, the flow kinematics, the rate of deformation within the fluid and the tensile force exerted on the end-plate. The fluid considered in this section is a polyisobutylene-based Boger fluid (PIB 0.31 wt.%). The basic geometric parameters and the material properties are listed in Table 1. The numerical simulation is based on an axi-symmetric model with 720 9-node quadratic elements giving a total number of unknowns of about 16 000
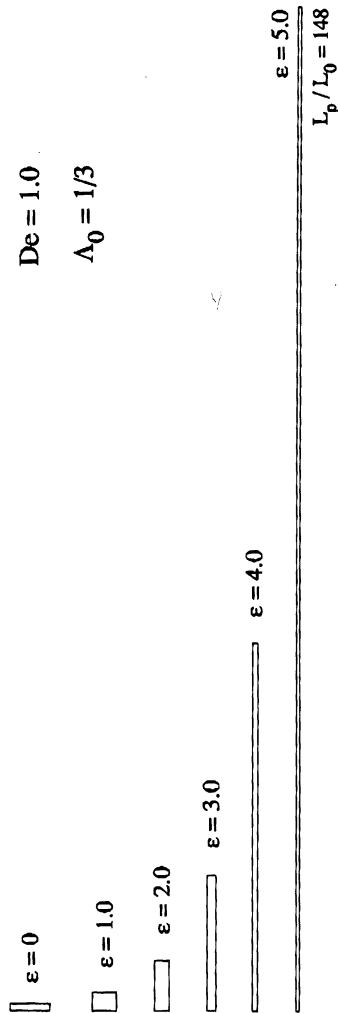
Fig. 2. Evolution of the computational domain during the large extensional deformations in the benchmark test with an exponentially reducing diameter at both end-plates. The left vertical boundary is the symmetry axis, the right vertical boundary is the free surface which remains cylindrical in this special case. The lower and upper horizontal boundaries are the stationary and moving end-plate, respectively.
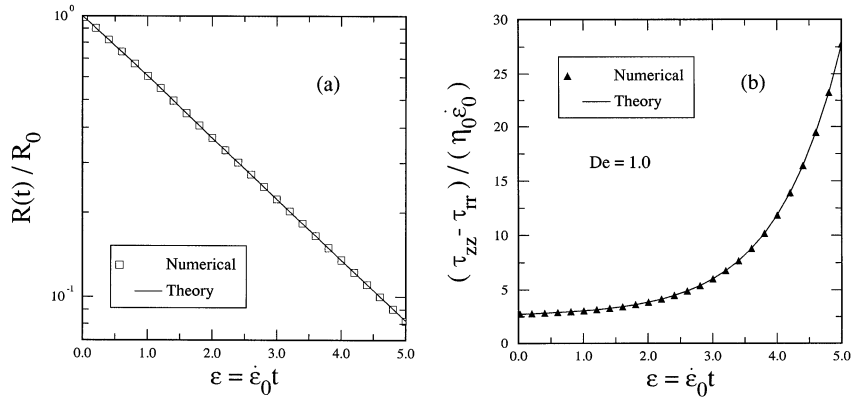
Fig. 3. Comparisons of numerical solution with theory for the benchmark test. The stretching rate is $\dot{\varepsilon}_0 = 0.394\ \text{s}^{-1}$ and the material properties of the PIB fluid are given in Table 1. The solid curves marked 'theory' denote the analytical solution for the transient start-up of uniaxial elongational flow of an Oldroyd-B fluid [11]. (a) The radial deformation history of free surface; (b) the Trouton ratio based on the first normal stress difference, $N_1 = T_{zz} - T_{rr}$, within the liquid bridge.

at each time-step. In the time marching, the size of time-step is selected in such a way that the implicit time integration always advances at an equal increment of strain, $\Delta\varepsilon = \dot{\varepsilon}_0\,\Delta t = 0.01$, for the various extension rates considered. A typical computation takes about $12 \sim 20$ h CPU time on an IRIX Power Challenge (MIPS R8000) machine.

4.1. Free surface deformation

One of the important features of the extensional deformations experienced by the liquid bridge in a filament stretching rheometer is the evolution and shape change of the free surface. In the conventional design, the free surface of the liquid column cannot remain cylindrical due to the pinning condition at the rigid end-plates, and deforms greatly during the stretching history. A typical free surface deformation history for an Oldroyd-B liquid bridge with a small initial aspect ratio $\Lambda_0 = 1/3$ is shown in Fig. 4. For comparison purpose, we also show the deformation of the corresponding Newtonian liquid bridge with the same initial aspect ratio and the same material properties of the solvent. Initially, the deformations of the viscoelastic and the Newtonian liquid bridges are almost identical at small strains as shown by the profiles at Hencky strains of $\varepsilon = 0.2$ and $\varepsilon = 1.0$. When the strain surpasses a critical value ε_p, in this particular case $\varepsilon_p \approx 1.75$, the viscoelastic liquid shows the onset of significant strain hardening which was first observed experimentally by Tirtaatmadja and Sridhar [4] and later by Spiegelberg et al. [9] at high Deborah numbers (De > 3). As a result of the strain hardening phenomenon, the 'necking' in the central part of the viscoelastic liquid bridge becomes slower than that in the Newtonian case. The Newtonian filament does not show any strain hardening, the radius is non-uniform at all times and the filament becomes very thin at $\varepsilon = 3.92$. By contrast in the viscoelastic liquid, the strain hardening leads to a progressively more uniform filament in the central part of the bridge. The strain hardening phenomenon shown in Fig. 4 agrees well qualitatively with the experimental observations reported in the literature.

In addition to the strain hardening phenomenon manifested near the axial mid-point of the filament, free surface deformations of viscoelastic liquids also differ dramatically from Newtonian liquids in the vicinity of the 'foot' area close to the end-plates when the strain becomes large, as indicated by the profiles at $\varepsilon = 3.92$ in Fig. 4. To examine the differences, the foot area near the fixed end-plate is enlarged in Fig. 5. The comparison shows that the free surface shapes of the Newtonian and the viscoelastic liquids are almost identical in a small local area around the tip of the end-plate. Consequently, the contact angle between the free surface and the end-plate is also nearly identical for both the Newtonian and the viscoelastic liquids in the special case modeled. The analysis by Gillette and Dyson [22] shows that for static liquid bridges the free surface shape is uniquely determined by the aspect ratio, the pressure difference and the volume of the liquid bridge. Even though the central portion of the elongating filament continues to undergo extensional deformations the liquid directly adjacent to the end-plates is prohibited by the no-slip boundary condition from flowing radially inwards and relaxes to a steady state in which the free surface near the outer rim is determined purely by capillary forces
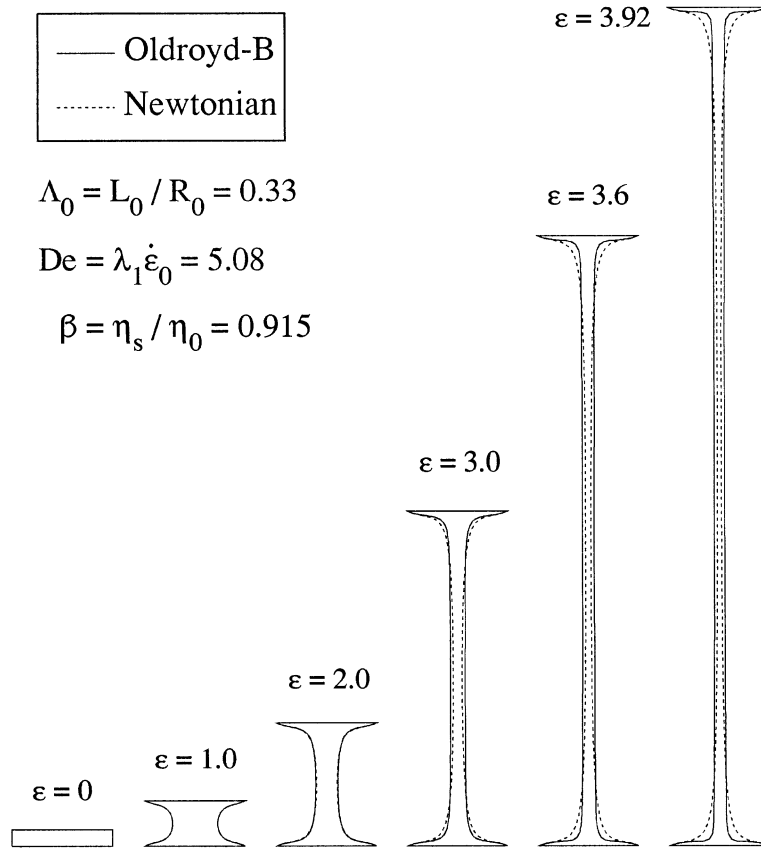
Fig. 4. Comparison of the predicted free surface profiles as a function of Hencky strain during extensional deformation of Newtonian (N) and viscoelastic (O–B) fluid filaments. The material properties of the PIB fluid are given in Table 1 and the stretching rate is $\dot{\varepsilon}_0 = 2.0\,\mathrm{s}^{-1}$ corresponding to De = 5.08 for the Oldroyd-B fluid.
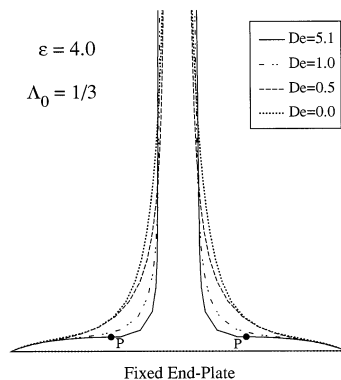
Fig. 5. An enlarged view of the extensional deformations in the local 'foot' area near the fixed end-plate for different Deborah numbers at a final strain of $\varepsilon \approx 4.0$.

at all De. The experimental curvature measurements near the bottom plate given by Spiegelberg et al. [9] also show that an essentially static fluid reservoir develops near the stationary end-plate with a time-invariant radius of curvature. Our numerical calculations appear to be physically consistent with the experimental measurements.

For Newtonian fluids, the free surface shape of this fluid reservoir closely resembles the neck of a bottle and the curvature of the free surface varies smoothly at the neck as shown in Fig. 5. Therefore the extensional deformations of a Newtonian liquid are relatively easier to handle for the remeshing algorithm and the flow solver. With the Thompson remeshing technique, large extensional strains, up to $\varepsilon \geq 5$, can be reached without difficulty. For viscoelastic liquids, however, calculations become more complicated since the axial curvature increases dramatically with De. As shown in Fig. 5, the curvature of the free surface changes dramatically with axial position at large strains and the fluid reservoir near the fixed end-plate is depleted of more fluid than in the Newtonian case. The viscoelastic behavior in this region poses a great challenge to numerical modeling, due to the fact that the finite elements used in the simulations are much more greatly distorted in the viscoelastic liquid bridge than in the Newtonian case. A closer analysis of the filament profile in Fig. 5 shows that the tangent of the free surface at the point P is almost parallel to the fixed end-plate. This leads to a very large curvature and hence very large values of the Jacobian in the finite element calculations. Experimental observations given by Spiegelberg et al. [10] show that further extensional deformation will further drain the liquid adjacent to the end-plate and initiate the onset of a non-axisymmetric elastic instability near the fixed end-plate, which results in the elongating fluid column partially decohering from the end-plate. Although it is impossible to unequivocally associate these numerical difficulties with the experimentally observed decohesion of viscoelastic filament, it is clear that filament stretching rheometers will face difficulties attaining very large strains of $\varepsilon > 5$. In numerical simulations, further extensional deformation will cause the point P to move towards the end-plate, and consequently the variation of curvature along the free surface will become non-monotonic and cannot be represented uniquely in the Mongé form $R(z, t)$. Hence for small initial aspect ratios $\Lambda_0 \ll 1$, numerical solutions for large extensional deformations are difficult to obtain and there exists an upper limit for the largest strain numerically achievable with the current formulation.

Our computational experience shows that the upper bound for numerical accessibility to large strains depends on several factors, including the initial aspect ratio, Deborah number, the viscosity ratio $\beta \equiv \eta_s/\eta_0$ and the constitutive model, etc. For the Oldroyd-B fluid model with $\Lambda_0 = 1/3$, $\beta = 0.91$ and De $= 5.1$, the highest Hencky strain achievable in our computation is about 4.0.

It is interesting to note that the configuration of the fluid reservoirs near the disks at high strain are affected not only by the viscoelastic stresses in the liquid, but also by the initial aspect ratio. Comparisons of surface shapes at three different aspect ratios are shown in Fig. 6 and suggest that the dramatic change in surface curvature can be effectively reduced with the increase of Λ_0. Therefore larger final strains ε_f can be obtained with larger initial aspect ratios. For example, when the initial aspect ratio is increased to $\Lambda_0 = 2/3$, the highest numerically-accessible Hencky strain is increased from $\varepsilon_f \approx 4.0$ to $\varepsilon_f \approx 4.4$ with the same β and De, and the same number of unknowns.

4.2. Radial flow kinematics

In ideal uniaxial elongational flow, the fluid kinematics are well known and the Eulerian solution in cylindrical coordinates is given by

$$
\left.
\begin{aligned}
u_r &= -0.5\dot{\varepsilon}_0 r, \\
u_\theta &= 0, \\
u_z &= \dot{\varepsilon}_0 z.
\end{aligned}
\right\}
\tag{26}
$$

Integration of the first equation in Eq. (26) gives

$$
R(t)/R_0 = \exp(-0.5\dot{\varepsilon}_0 t),
\tag{27}
$$

which describes the uniform radial displacement of the cylindrical free surface in ideal uniaxial elongational flow.

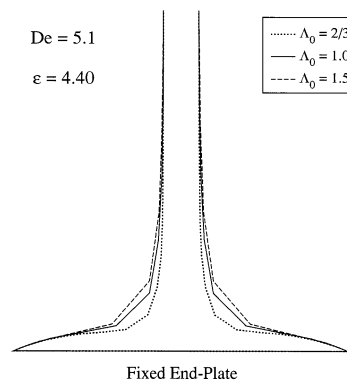For liquid bridges with fixed end-plates, the displacement of fluid elements on the free surface

Fig. 6. Effects of the initial aspect ratio $\Lambda_0 \equiv L_0/R_0$ on the extensional deformation and free surface shapes of viscoelastic liquid bridge in the 'foot' area near the end-plate.

(as well as within the entire domain) is temporally and spatially non-homogeneous. The radial movement at the two ends of the liquid bridge is completely restrained due to the pinning conditions at the fixed end-plates. As a result, the decrease of the radius at the central part of the filament is much faster than in ideal uniaxial elongational flow so that the volume of the bridge is conserved. Consequently, the flow kinematics in the liquid bridges with fixed end-plates is much more complicated and deviates significantly from the flow field given in Eq. (26). The presence of a deforming free surface whose position is unknown a priori means that exact analytical solutions for the velocity field are not available for either the Newtonian and viscoelastic liquid bridge problems, and the flow field in general can only be computed numerically.

However, an approximate analytical solution has been obtained for the initial response of a Newtonian liquid bridge based on lubrication theory [9]. This solution is valid for small aspect ratios ($\Lambda_0 \ll 1$) and viscous liquid filaments (Re $\ll 1$) at short times when the free surface is approximately cylindrical. This lubrication theory solution is very similar to that in the classical squeeze film problem of Stefan [11,23]. The major difference is that the direction of motion is reversed in the liquid bridge case and the boundary motion increases exponentially in time. The axial and radial velocity components of the lubrication theory solution are described by the following simple expressions in dimensional form

$$u_r = -3\dot{\varepsilon}_0 r \left(1 - \frac{z}{L_\mathrm{p}}\right)\frac{z}{L_\mathrm{p}}, \qquad u_z = \dot{L}_\mathrm{p}\left(3 - 2\frac{z}{L_\mathrm{p}}\right)\left(\frac{z}{L_\mathrm{p}}\right)^2, \tag{28}$$

which satisfies the velocity boundary conditions at the two end-plates, but does not satisfy the stress boundary conditions on the free surface. However, since the Capillary number Ca $\gg 1$ in most tests this error is small. Although Eq. (28) is derived for Newtonian liquids, it should also be a good approximation for Oldroyd-B liquid bridges at small strains based on the squeeze flow experiment and calculations by Phen-Thien and Boger [24,25]. In addition, experimental observations in filament stretching devices [9] also show that the fluid response is Newtonian for $\varepsilon < 1$. Setting $z = L_\mathrm{p}/2$ in Eq. (28) and integrating u_r suggest that the mid-point of fluid filament should initially decrease as

$$R_\mathrm{mid}(t)/R_0 = \exp(-0.75\dot{\varepsilon}_0 t). \tag{29}$$

By substituting Eq. (28) into Eq. (10), we obtain the following expression for the rate of deformation tensor

$$D_{zz} = 6\dot{\varepsilon}_0\left(1 - \frac{z}{L_\mathrm{p}}\right)\frac{z}{L_\mathrm{p}}, \qquad D_{rz} = -3\dot{\varepsilon}_0\left(1 - 2\frac{z}{L_\mathrm{p}}\right)\frac{r}{L_\mathrm{p}}. \tag{30}$$

The lubrication solution predicts that D_{zz} is parabolic in the axial direction with a maximum value at $z/L_\mathrm{p} = 0.5$ of

$$D_{zz} = 1.5\dot{\varepsilon}_0. \tag{31}$$

The results in Eqs. (29) and (31) suggest that at the very beginning of the deformation the fluid element at the mid-point section experiences a local extensional strain rate which is about 50% higher than the imposed global strain rate $\dot{\varepsilon}_0$; however the average of D_{zz} along the axial direction is still the same as the imposed $\dot{\varepsilon}_0$.
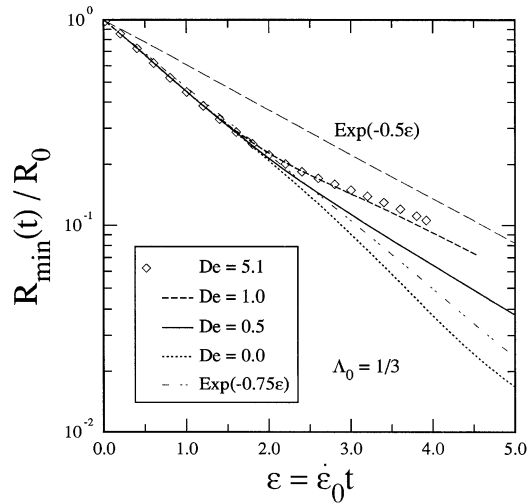
Fig. 7. Variation of the minimum radius of the liquid column, $R_{\min}$, with respect to the imposed axial Hencky strain, $\varepsilon = \dot{\varepsilon}_0 t$, and as a function of Deborah number. De = 0 is the corresponding Newtonian case. The geometrical and material parameters for the PIB fluid used are the same as given in Table 1.

To quantify the extensional deformation at the central part of the filament, we show the computed time history of the minimum radius, $R_{\min}(t)$ as a function of Hencky strain in Fig. 7. The lubrication prediction in Eq. (29) is in good agreement with the computed rate of decrease observed in the Newtonian filament at all strains up to $\varepsilon = 2.5$ as shown by the zero De curve in Fig. 7. For larger strains $\varepsilon > 2.5$, the necking in $R_{\min}$ accelerates slightly and eventually leads to a capillary instability in the vicinity of the mid-plane of the Newtonian liquid bridge. For viscoelastic filaments, there are in general two distinct regions in the curve of $R_{\min}(t)$. In the first region, corresponding to strains $\varepsilon < 1.75$, the evolution in $R_{\min}$ is the same as Newtonian and the filament undergoes significant necking as observed in Fig. 4. This result agrees well with the conclusions made in the literature [24,25] that the initial behavior of the Oldroyd-B fluid during squeeze flow is basically that of the Newtonian solvent contribution. The second region for strains $\varepsilon > 1.75$ is characterized by a slope change in the curve of $R_{\min}(t)$. In this region the radius decreases more slowly than that in the ideal uniaxial elongational flow due to strain hardening in the fluid. This characteristic change in the slope shown in Fig. 7 agrees well with the experimental measurements shown in [2,3,7,9].

The radial free surface displacement in the central part of the filament is greatly affected by the initial aspect ratio. Typical results are presented in Fig. 8 in which the minimum filament radius $R_{\min}$ is plotted versus Hencky strain for three different aspect ratios $\Lambda_0 = 2/3$, $3/2$ and 2. All the three curves fall into a region bounded from below by the lubrication solution Eq. (29) and from above by the ideal uniaxial elongational flow solution Eq. (27). Note that the lower limit curve corresponds to larger radial displacement and higher radial velocities, while the upper limit curve represents the smaller radial displacement and slower radial velocity that the particle would experience in an ideal uniaxial elongational flow. The results in Fig. 8 show that the change of slope arising from strain hardening become less significant for liquid bridges with larger initial aspect ratios. At $\Lambda_0 = 2$, the slope change in the $R_{\min}$ curve is much smaller than

that for $\Lambda_0 = 2/3$, and the radial deformation is much closer to the ideal curve $R(t)/R_0 = \exp(-0.5\varepsilon)$. The trend indicated in Fig. 8 provides useful information for design of future experiments, namely a more effective design strategy is to choose larger initial ratios of the liquid filament.

The lubrication solution given in Eq. (28) predicts that the axial velocity is a cubic function of z and the radial velocity is a parabolic function of z, whereas the ideal uniaxial elongational flow described by Eq. (26) has a linear variation in z for u_z and a constant value for u_r. Comparisons of the numerical simulation for the Newtonian and Oldroyd-B fluids with these predictions are presented in Figs. 9 and 10. The axial velocity profile along the centerline $r = 0$ and the radial velocity profile on the deformed free surface ($r = R(z, t)$) respectively are plotted over a range of strain levels.

In general, the flow in the liquid bridge differs from the ideal uniaxial elongational flow, except in the immediate vicinity of the mid-point section $z = L_{\mathrm{p}}/2$ where the agreement is purely a result of geometric symmetry. For the Newtonian liquid, the lubrication solution provides a surprisingly good approximation for u_z up to $\varepsilon \approx 2.0$, and the agreement is still fairly good even for larger strains up to $\varepsilon = 3.8$, as shown in Fig. 9. For Oldroyd-B fluid, the lubrication solution of u_z is a very good approximation for $\varepsilon \leq 1.0$. For $\varepsilon > 1.0$, the flow behavior of the Oldroyd-B model starts to deviate gradually from that of Newtonian liquid, and the lubrication prediction becomes increasingly invalid.

The change in the deformation characteristics documented in Figs. 7 and 8 for the viscoelastic filaments is also manifested in Figs. 9 and 10. At strain levels $\varepsilon > 2.0$, the axial velocity near both end-plates dramatically changes. The velocity gradient $\partial u_z/\partial z$ at the mid-plane ($z/L_{\mathrm{p}} = 0.5$) decreases below both the lubrication solution and the ideal homogeneous uniaxial elongation due to the onset of strain-hardening. By contrast, near the end-plates ($z/L_{\mathrm{p}} = 0, 1$), the axial velocity gradient dramatically increases indicating that fluid is progressively drained out of the 'foot' or reservoir region.
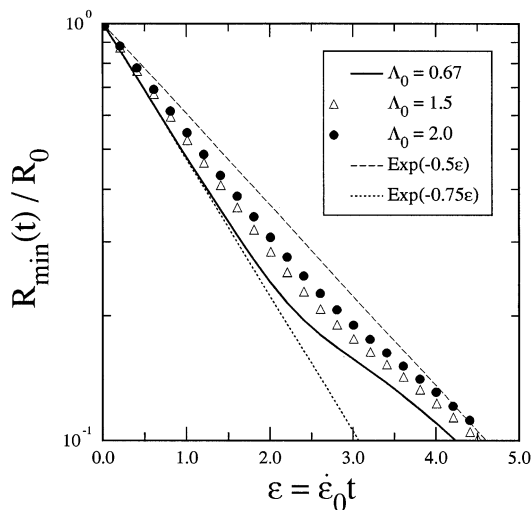

Fig. 8. Effects of the initial aspect ratio on the radial deformation of the viscoelastic liquid bridge as a function of the imposed global Hencky strain, ε.
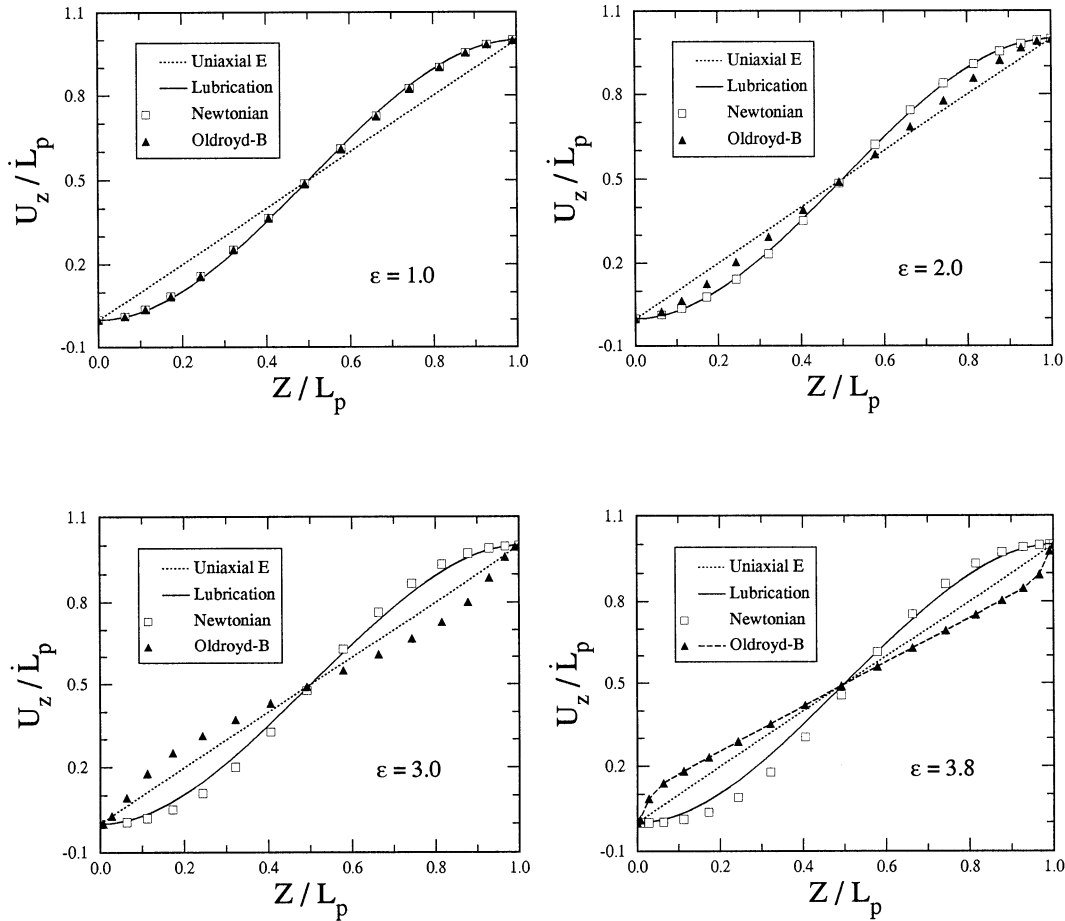
Fig. 9. Profiles of the axial velocity along the centerline of the liquid bridge at four typical strain levels. Numerical solutions of the Oldroyd-B and the Newtonian liquids are compared with the ideal uniaxial elongational flow (dot curves) and the lubrication solution given by Eq. (28) (solid curves). The same initial aspect ratio $\Lambda_0 = 1/3$ and extension rate $\dot{\varepsilon}_0 = 2 \, \mathrm{s}^{-1}$ were used for both the Newtonian and viscoelastic cases which leads to De = 5.08 for the latter simulation.

Comparisons with numerical simulations also indicate that the lubrication solution provides an accurate description of the radial velocity profile along the free surface, at least at small strains, as shown in Fig. 10. In the uniaxial elongational flow, u_r is homogeneous in space, by contrast in the filament stretching devices, u_r is non-homogeneous due to the boundary conditions imposed by the end-plates. For viscous Newtonian liquids with material properties typified by those in Table 1, the lubrication solution appears to be a fairly good approximation even at large strains up to $\varepsilon = 3.8$ except very close to the pinned contact regions. Here the velocity gradient $\partial u_r / \partial z$ decreases to zero confirming that the region becomes quasi-static. For the Oldroyd-B fluid, the radial velocity of the free surface gradually decreases at strains $\varepsilon > 1.75$ and becomes increasingly axially uniform in the central part of the domain. For $\varepsilon \geq 3.0$, the

radial inflow in the central region of the free surface becomes slower than that in the ideal uniaxial elongational flow, indicative of appreciable strain hardening. At $\varepsilon \geq 3.8$, a homogeneous radial velocity profile is achieved over most of the liquid bridge. Concomitantly, velocity
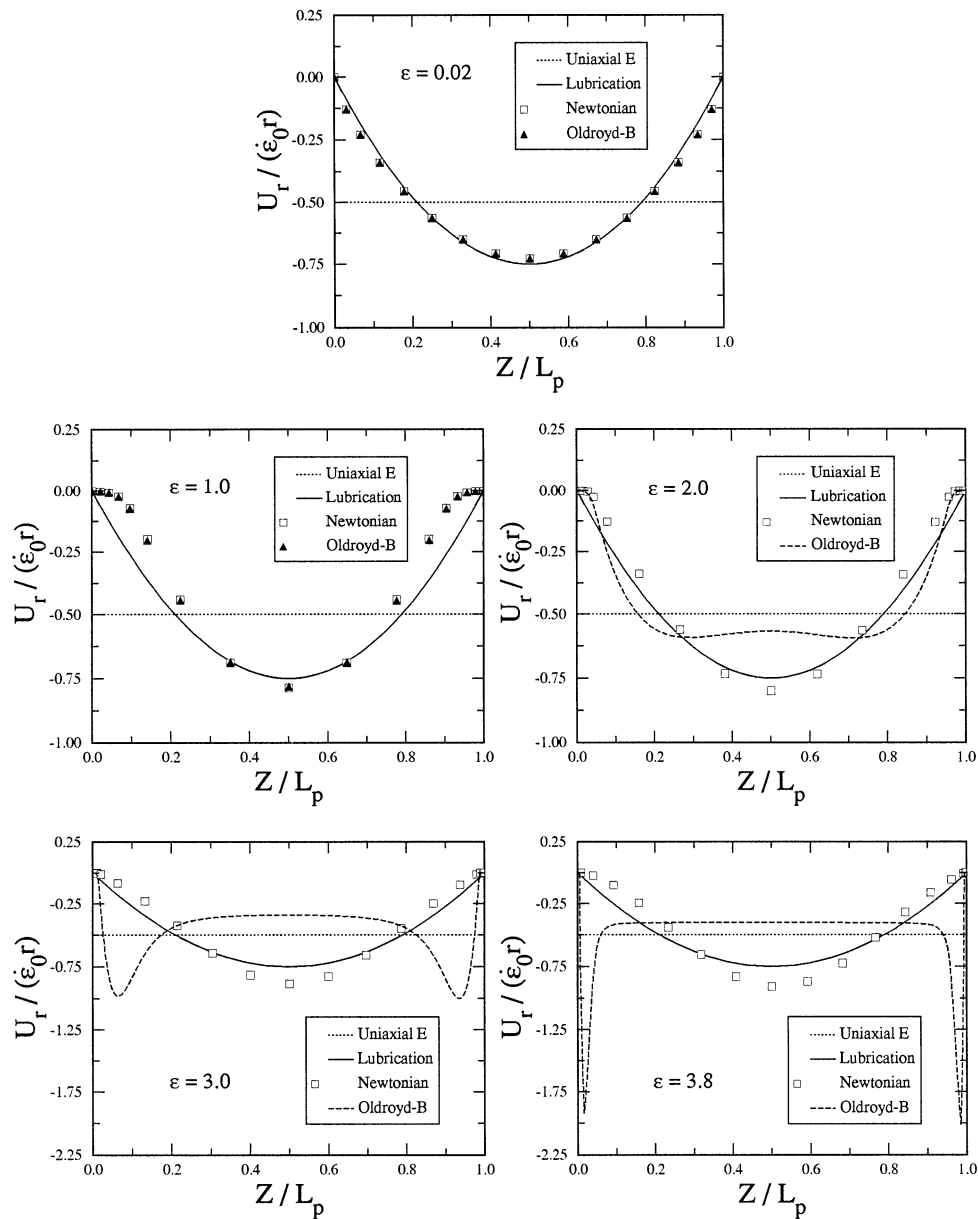

Fig. 10. Profiles of the radial velocity on the free surface $r = R(z, t)$ at selected values of Hencky strain, $\varepsilon = \dot{\varepsilon}_0 t$. The results are based on a small initial aspect ratio $\Lambda_0 = 1/3$ and an extension rate $\dot{\varepsilon}_0 = 2 \text{ s}^{-1}$. The non-Newtonian case corresponds to a Deborah number of De = 5.08.

boundary layers develop near the two end-plates at high strains. These velocity boundary layers further contribute to the dramatic difference between viscoelastic and Newtonian liquids in free surface shapes near the foot area as discussed above in Section 4.1. Resolution of these boundary layers contributes to the difficulties in attaining high strains numerically.

4.3. Rate of deformation

The deformation history of the liquid bridge can also be quantitatively characterized by the extensional and shear strain rates which represents the deformation rate that the fluid elements experience during the stretching process. The spatial and temporal variations of strain rates can be used in error control for quantifying inhomogeneities and deviations of the real flow field from the ideal uniaxial elongational flow. Ideally, we would like to control the actual strain rate to be purely extensional, homogeneous and identical to the imposed value of $\dot{\varepsilon}_0$. However, as we have shown, the actual strain rate is not that expected in a simple extensional flow and, in general, it varies both spatially and temporally. Since direct measurement of the detailed distribution of strain rate within the liquid bridge is very difficult, numerical simulation plays an important role in studying the rate of deformation and provides some interesting insight into the flow field.

For the cylindrical coordinate system shown in Fig. 1, the rate of deformation tensor $\boldsymbol{D}$ defined in Eq. (10) has four independent non-zero components: D_{rr}, D_{rz}, D_{zz} and $D_{\theta\theta}$, all of which vary with spatial position and time. Among them, the components D_{zz} and D_{rz} are of most interest to our study since they characterize the extension rate and the shear rate in the fluid. For a homogeneous uniaxial elongational flow given by Eq. (26), $D_{zz} \equiv \dot{\varepsilon}_0$ and $D_{rz} \equiv 0$. When the end-plate diameter is fixed as in conventional stretching devices, the flow field is altered by the pinning conditions at the rigid end-plates, as a result, D_{zz} becomes a function of time and space. It is interesting to note the value of $\boldsymbol{D}$ at the rigid end-plates. For incompressible fluids, it is easy to prove from the no-slip boundary condition and the continuity equation that

$$D_{rr} = D_{zz} \equiv 0. \quad \forall \{(r, z) | z = 0 \quad \text{or} \quad z = L_{\mathrm{p}}\}. \tag{32}$$

Boundary layers in the velocity gradients (and associated stresses) thus develop near the rigid fixtures. For the Oldroyd-B fluid, typical spatial and temporal variations of D_{zz} and D_{rz} are shown in the contours plots presented in Fig. 11. The actual extensional strain rate within the liquid bridge is highly non-homogeneous at the initial stage of stretching as seen from the contours plots of $\varepsilon = 0.2$ and 1.0 in Fig. 11(a). At $\varepsilon = 0.2$, the contours are almost parabolically distributed in the axial direction and radially uniform as expected from Eq. (30). However, the non-homogeneity is gradually reduced with increasing strain and a homogeneous deformation zone (HDZ) is formed at the central part of the domain as shown by the plot of $\varepsilon = 2$ in Fig. 11(a). Our simulation shows that this HDZ continues to expand towards the two end-plates with further stretching and strain-hardening in the fluid. The contour plot of D_{rz} at $\varepsilon = 0.2$ in Fig. 11(b) suggests that a significant shearing component is generated between the plates at small strains. As shown in Fig. 11(b), the shear rate is negligibly small in the central part of the liquid bridge but is largest near the pinned free surface. Subsequent contour plots in Fig. 11(b) indicate that the shear rate decays rapidly with the increase of strain.

As we have shown in Fig. 9, the lubrication prediction (derived in the limit $\Lambda_0 \ll 1$) remains a good approximation even up to strains of $\varepsilon \sim 1.75$ for both the Newtonian and Oldroyd-B
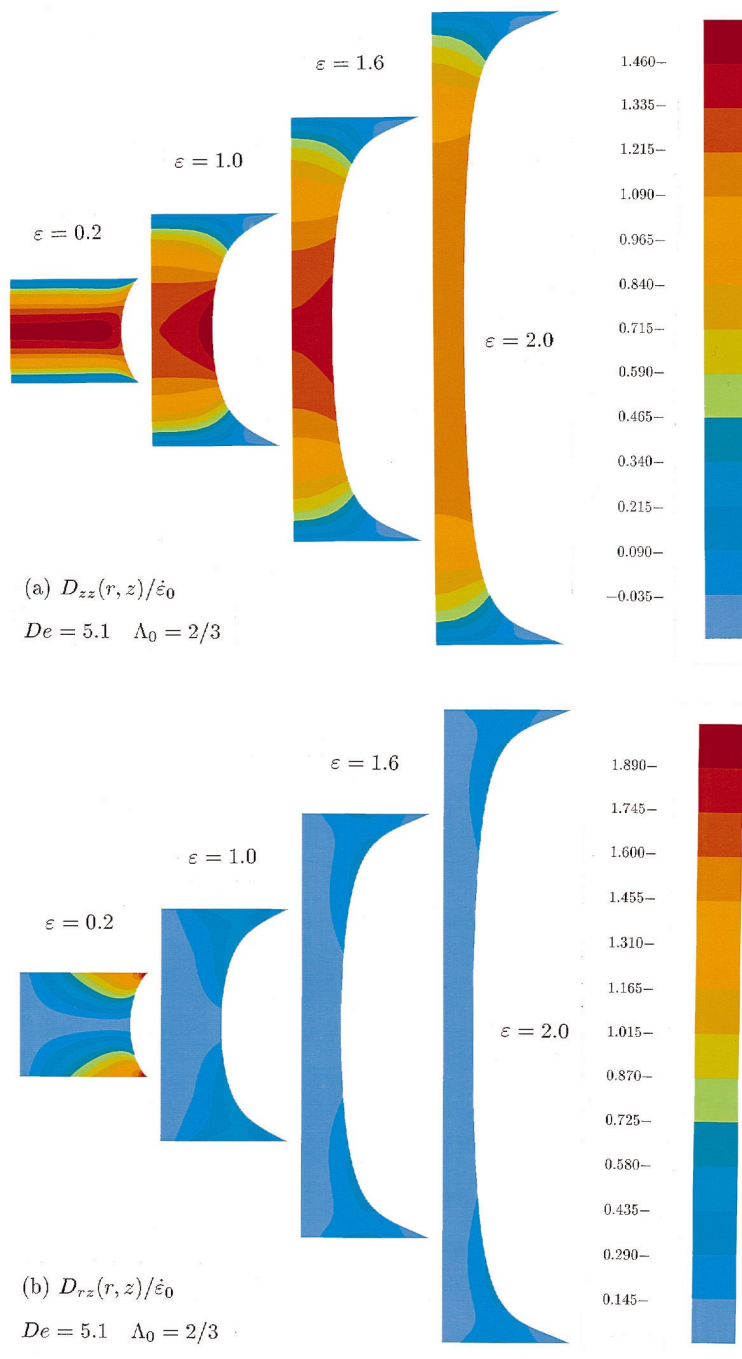
Fig. 11. Contour plots of components of the rate of deformation tensor at four selected strain levels, $\varepsilon = 0.2$, 1.0, 1.6 and 2.0, respectively. The results are based on the half-domain model of the Oldroyd-B liquid bridge with $\Lambda_0 = 2/3$ and De = 5.08. (a) The axial velocity gradient D_{zz}; (b) the shear velocity gradient D_{rz}.

fluids. Beyond this range, the extensional behaviors of the two liquids become significantly different. For Newtonian filaments within a strain range $1.5 < \varepsilon < 4$, the extensional strain rate at the mid-point section tends to increase slightly with strain due to the increasing capillary pressure and the maximum axial velocity gradient D_{zz} remains at the mid-plane of the filament where the radius is smallest. For Newtonian liquid bridges, there is no strain hardening and the necking is always largest at the mid-plane between the two end-plates. Consequently, although we do not resolve the dynamics of the actual filament breakup process, our numerical modeling indicates that the Newtonian liquid bridges in conventional filament stretching devices will break in the middle, which agrees well with experimental observations. For the viscoelastic fluid, strain hardening becomes important at large strains and strain rates due to the elongation of the polymer chains. As a result, the extensional strain rate in the central part of liquid bridge decreases gradually and two boundary layers in D_{zz} are simultaneously developed near the two end-plates as indicated by the plots of $\varepsilon = 3$ and 3.8 in Fig. 9. Physically, the strain-hardening liquid in the middle of the column becomes increasingly difficult to stretch, and it becomes relatively easier to pull the unstretched material out of the fluid reservoir in the 'foot' areas adjacent to the two end-plates. With the development of the two boundary layers, the extensional strain rate is increased rapidly near the two end-plates. At $\varepsilon = 3.8$, the maximum values of D_{zz} are about 4.5 times larger than the imposed global extensional rate $\dot{\varepsilon}_0$ and continue to increase dramatically with further stretching. The break-up mechanism in viscoelastic liquid bridge at high De is thus anticipated to be quite different from the Newtonian case. The strain hardening and viscoelastic behavior of the fluid prevent the filament from breaking in the middle. Instead, the increasingly rapid rate of liquid drainage from the 'foot' regions leads to a uniform elastic column connected by a thin fluid film to the rigid end-plate. Numerical calculations show that the radius of curvature in these regions becomes very small and large (negative) pressure gradients develop as the filament elongates. Ultimately the slope $\partial R/\partial z$ of the free surface becomes almost zero near the end-plates and numerical convergence is lost. Although we do not directly simulate the elastic instability, this sequence appears to be consistent with recent experimental observations of elastic filament break-up and decohesion [10].

Since the lubrication solution Eq. (28) does not satisfy the boundary conditions at the free surface, it should not be expected to accurately describe the kinematics near the free surface. To demonstrate this, we show in Fig. 12 the radial variation of the dimensionless axial strain rate $D_{zz}/\dot{\varepsilon}_0$ at the mid-plane of the elongating filament $z = L_{\mathrm{p}}(t)/2$. At very short times the filament is still almost cylindrical and the radial shear flow in the bridge is driven by the radial pressure gradient in the bulk. As a result, the extensional strain rate at the free surface ($r = R(z, t)$) is almost zero, as shown by the curve at $\varepsilon = 0.02$ in Fig. 12. As the free surface deformation increases, the value of D_{zz} at the mid-point of the free surface increases rapidly in a short time and a boundary layer develops as indicated by the curve at $\varepsilon–0.2$ in Fig. 12. The lubrication solution cannot predict this boundary layer but agrees well with full numerical simulation in the central core area $r < 0.7R(t)$. After this initial deformation, the value of D_{zz} at the mid-point of the free surface gradually decreases. At $\varepsilon = 2$, the boundary layer completely disappears. At strains $\varepsilon > 2$, the extension rate is radially homogeneous and approaches the imposed global extension rate. Despite the homogeneity of the deformation rate at high strains, we show below in Section 4.4 that the viscoelastic fluid filaments exhibit a 'memory' of this initial inhomogeneity that is manifested in a radial stress boundary layer at all strains.
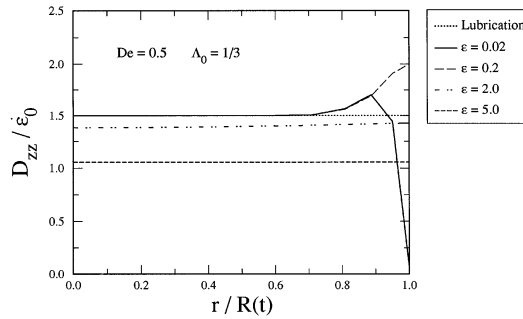
Fig. 12. The radial variation of D_{zz} on the mid-plane, $z = L_p/2$, at four selected strain levels and comparison with the lubrication solution. The numerical solution satisfies the free surface boundary conditions at $R_{mid}(t)$ while the lubrication solution does not.

Further consideration of Fig. 12 and examination of additional plots of the radial velocity profile in the filament mid-plane (not shown here) help explain why the lubrication solution derived in the limit $\Lambda_0 \ll 1$ provides a good description of the filament profile and fluid kinematics even at aspect ratio, $\Lambda_t = \Lambda_0 e^{+\varepsilon} > 1$. The linear variation in the radial fluid velocity and the radial uniformity in the axial strain rate at each axial position indicate that the velocity field at high strains can be expressed in the form

$$u_z = V_0 f(z) \, e^{+\dot{\varepsilon}_0 t} \quad \text{and} \quad u_r = -\frac{r}{2} V_0 f'(z) \, e^{+\dot{\varepsilon}_0 t}, \tag{33}$$

where $f(z)$ is an unknown function of z to be determined from the momentum equation and boundary conditions, $V_0 = \dot{\varepsilon}_0 L_0$ is the initial velocity of the moving plate and $f'(z) = df/dz$. This spatial variation in the kinematics (without the exponential weighting imposed by the end-plate boundary condition) is of the general slender-body form used to describe slender Newtonian and non-Newtonian filaments in, for example, fluid jets (see e.g. [26–28]). The lubrication solution obtained at short times, Eq. (28), is also exactly of this same form with a specific cubic polynomial representation:

$$f(z) = \left[3 - 2 \left(\frac{z}{L_p} \right) \right] \left(\frac{z}{L_p} \right)^2, \tag{34}$$

and the kinematics of the elongating filament are therefore of the same general form throughout the entire experiment.

4.4. The effective extensional strain rate

A more practical way to quantify the rate of deformation in the elongating liquid filament is via the local extensional strain rate at the mid-plane or the minimum radius plane. For example, as proposed in the literature [5,9], the local extensional strain rate at the mid-plane between the two end-plates can be quantitatively characterized on the basis of the free surface movement by the effective extension rate:

$$\dot{\varepsilon}_{\text{eff}} \equiv -2d(\ln R_{\text{mid}})/\mathrm{d}t = -2U_{r,mid}/R_{\text{mid}}, \tag{35}$$

where $U_{r,\text{mid}}$ is the radial velocity component of the free surface at the mid-plane. The first equality in Eq. (35) is widely used in experiments since R_{mid} can be obtained directly from the measured free surface shape. The second equality is convenient for numerical analysis when the velocity-pressure formulation is used. The effective extension rate represents the actual local extensional strain rate of fluid elements in the vicinity of the mid-plane (or the minimum radius plane). To demonstrate how the local extensional strain rate varies with strain, a typical example is presented in Fig. 13 for a low Deborah number of De = 0.5. In this example, the local extensional strain rate at the mid-plane is calculated using: (1) the effective extension rate $\dot{\varepsilon}_{\text{eff}}$ based on the free surface movement; (2) the average axial velocity gradient $\bar{D}_{zz}$ averaged over the mid-plane, $\bar{D}_{zz} = 2 \int_0^{R_{\text{mid}}} r D_{zz}[r, L_{\text{p}}(t)/2)] \, \mathrm{d}r / R_{\text{mid}}^2$; (3) the pointwise value of D_{zz} evaluated at the central point $r = 0$ and $z = L_{\text{p}}/2$. As shown in Fig. 13, the effective extension rate defined in Eq. (35) approximates the average of D_{zz} at the mid-plane very well throughout the stretching process. Therefore, the numerical computations verify that $\dot{\varepsilon}_{\text{eff}}$ does indeed represent the actual extensional strain rate that the fluid particles experience at the mid-plane. The difference between the values of $\dot{\varepsilon}_{\text{eff}}$ and the 'pointwise' D_{zz} curves at $\varepsilon \leq 2$ indicates that the extensional strain rate is non-uniform on the mid-plane with lower values at the center, which is consistent with the results shown in Fig. 12. The pointwise value of D_{zz} shown in Fig. 13 agrees well with the lubrication prediction $\dot{\varepsilon}_{\text{eff}} = 1.5\dot{\varepsilon}_0$ within the small strain range $0 < \varepsilon < 0.75$, which confirms once again that the lubrication solution can be used to characterize the fluid behavior at the central core part of the liquid bridge for small strains. At larger strains when $\varepsilon > 2$, all three curves merge together suggesting that a radially homogeneous extensional strain rate is achieved. At De = 0.5, no significant strain hardening is shown and the extensional strain rate at the mid-plane gradually approaches the imposed global strain rate $\dot{\varepsilon}_0$ with increasing strain. This calculation illustrates that axial homogeneity of the extensional strain rate is much harder
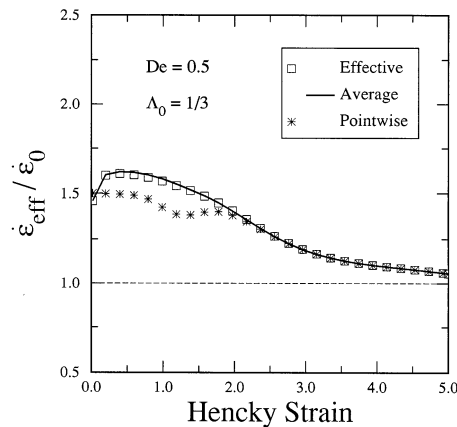

Fig. 13. Variation of the local extensional strain rate at the mid-plane between the two end-plates at low Deborah number De = 0.5. The local strain rate is characterized by the effective extensional strain rate, $\dot{\varepsilon}_{\text{eff}}$ ($\square$), the average value of D_{zz} over the mid-plane (——) and the pointwise value of D_{zz} at the center of the liquid bridge, $r = 0$, $z = L_{\text{p}}/2$ (∗).
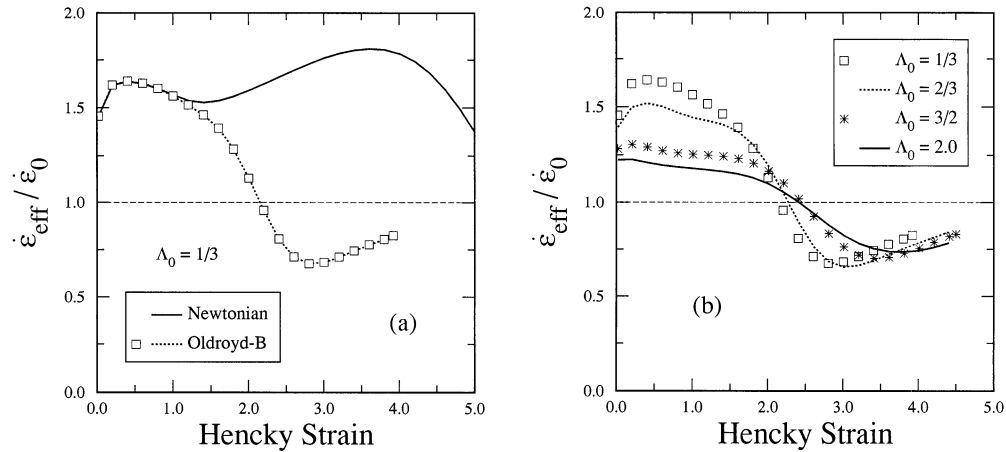
Fig. 14. Variation in the effective extensional strain rate computed by using Eq. (35) at large Deborah numbers. (a) Comparison of viscoelastic behavior with Newtonian response at a small initial aspect ratio of 1/3; (b) comparison of four different initial aspect ratios for the viscoelastic liquid bridge. The imposed global extension rate is $\dot{\varepsilon}_0 = 2 \text{ s}^{-1}$ (De = 5.08) in all the cases.

to achieve than a uniform radial profile and requires much larger strains ($\varepsilon > 5$) in filament stretching devices.

The variation in the calculated effective extensional strain rate at a much higher Deborah number of De = 5.1 is shown in Fig. 14(a). In this case, the strain hardening for $\varepsilon > 2$ can be clearly quantified by the rapid decrease in the value of $\dot{\varepsilon}_{\text{eff}}$. A comparison to the corresponding Newtonian case is also presented in Fig. 14(a) with the same initial aspect ratio and imposed stretch rate $\dot{\varepsilon}_0$. The extensional behavior of the Newtonian liquid shows significant differences from that of its viscoelastic counterpart. It is also clear from Fig. 14(a) that the effective stretch rate based on the change in radius of the mid-plane in the Newtonian filament never approaches the imposed value $\dot{\varepsilon}_0$. Direct calculation of a Trouton ratio based on the known solvent viscosity and the imposed stretch rate (i.e. $\text{Tr} = (\tau_{zz} - \tau_{rr})/\eta_s \dot{\varepsilon}_0$) will never return a value $\text{Tr} = 3$ but rather $\text{Tr} = 4.5$ due to the increased stresses near the filament mid-plane. This important computational result is analogous to the findings of numerical studies of the opposed jet devices which show that in this configuration Newtonian fluids yield a measured Trouton ratio of $\text{Tr} = 4.0$ [14]. A quantitative comparison of the effects of the initial aspect ratio on the calculated $\dot{\varepsilon}_{eff}$ is presented in Fig. 14(b). The comparison suggests that both the magnitude of the deviation in $\dot{\varepsilon}_{\text{eff}}/\dot{\varepsilon}_0$ and the temporal variation of the extensional strain rates attained in the bridge can be effectively improved by increasing the initial aspect ratio Λ_0.

4.5. Stress distribution and surface boundary layers

In an ideal uniaxial elongational flow, the stress is spatially homogeneous throughout the elongating filament. In filament stretching devices, however, the stress varies both axially and radially due to the non-homogeneous flow kinematics introduced by the end-plate conditions.

Numerical simulations can provide detailed information about stress distributions within the liquid. These detailed stress distributions are in general not available from direct measurements.

In Figs. 15 and 16, we show the contours of the total extra stress component τ_{zz} and τ_{rz} for a typical Oldroyd-B liquid bridge and its corresponding Newtonian counterpart. The initial aspect ratio and the imposed global extension rate used in the computation are $\Lambda_0 = 1/3$ and $\dot{\varepsilon}_0 = 2 \, \text{s}^{-1}$. Quantitative comparisons of the axial and radial variations in τ_{zz} are also presented in Figs. 17 and 18. For small strains, the stress distribution of the Oldroyd-B fluid is almost identical to that of the Newtonian fluid, as shown by the contour plots at $\varepsilon = 0.2$ in Figs. 15 and 16. Initially, τ_{zz} has a parabolic profile along the centerline of the liquid bridge with a vanishing value at the end-plates and a local maximum value at the mid-point. The full numerical solution agrees well with the lubrication approximation as shown in Fig. 18(a).

For viscoelastic filaments, the polymeric stress grows with the increase of strain and provides extra resistance to the extensional deformation. As a result of the spatially inhomogeneous deformation at short times shown in Figs. 12, 15 and 16, a region of stress concentration or 'boundary layer' is developed in the extra tensile stress τ_{zz} near the axial mid-point of the free surface as shown by the red colored areas in Fig. 15. In the experiments, such radial stress distributions within the liquid filament are almost impossible to measure, even with a line-of-
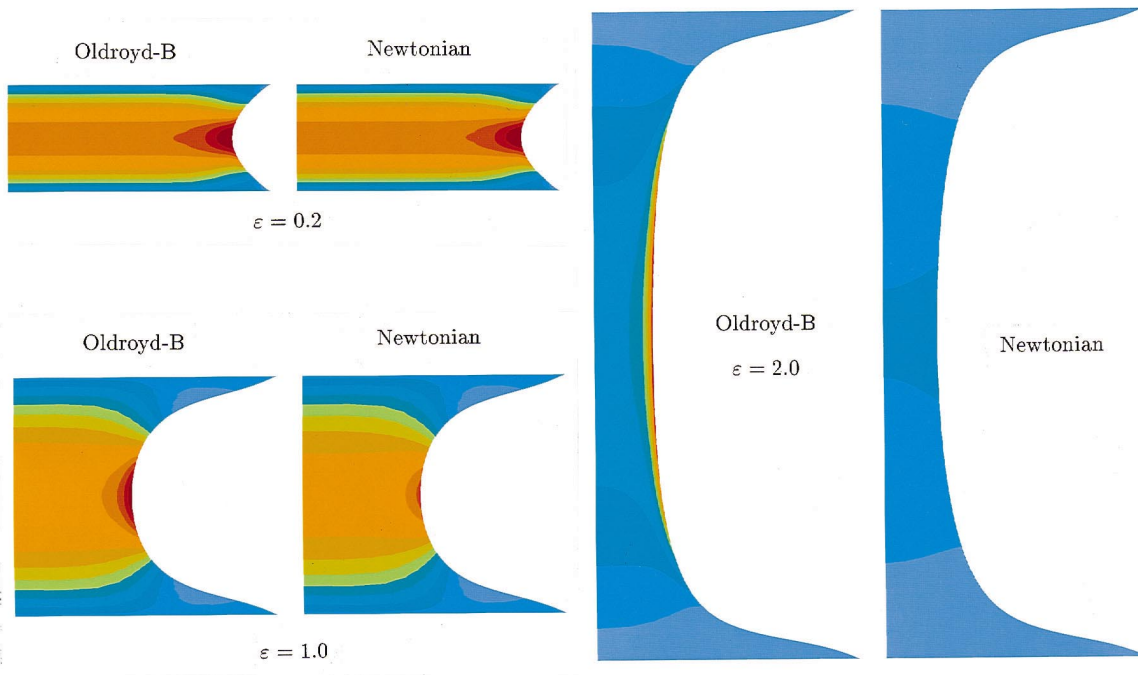

Fig. 15. Contour plots of the extensional component of the total extra stress, τ_{zz}, defined in Eq. (7). Comparison of Oldroyd-B model (De = 5.08) with Newtonian liquid. The left vertical boundary is the symmetric axis ($r = 0$), the right curved boundary is the free surface, top boundary is the moving end-plate and bottom line is the fixed end-plate. The color table of the contour plots has 13 colors with equal increment in stress levels. The red and gray colors represent the highest and lowest stress levels respectively.
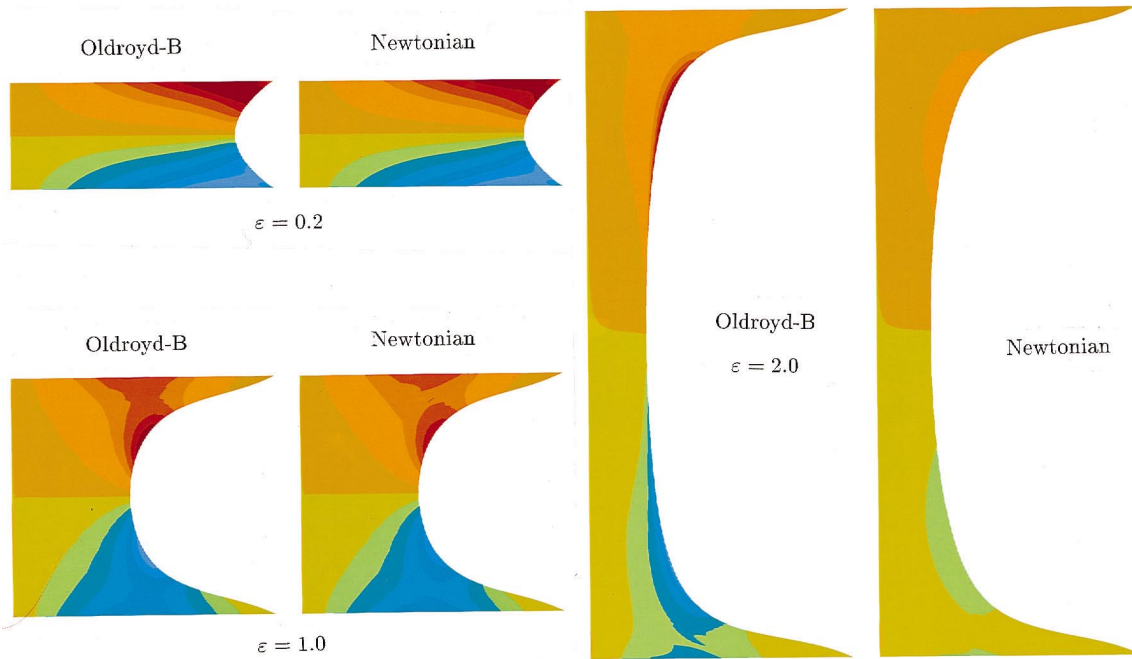
Fig. 16. Contour plots of the shear component of the total extra stress tensor, τ_{rz}. Comparison of Oldroyd-B model (De = 5.08) with Newtonian liquid. Since the shear stress is anti-symmetric with respect to the mid-plane, the red and gray colors represent identical magnitudes of τ_{rz} but with opposite signs.

sight technique such as birefringence, and force or birefringence measurements are interpreted as resulting from a radially uniform fluid stress. The numerical results predict an important difference in the stress behavior between the viscoelastic and the Newtonian liquids. For Newtonian liquids, the local stress concentration in the vicinity of the mid-point of the free surface is present only at small strains and eventually decays at larger strain levels as the instantaneous extensional strain rate $D_{zz}(r)$ becomes uniform across the mid-plane. For the Oldroyd-B fluid with a small initial aspect ratio, the local stress concentration induced at short times grows with strain throughout the deformation history and leads to a thin boundary layer at larger Hencky strains even when a homogeneous extensional strain is reached. This is a consequence of the viscoelastic memory of the fluid to its previous deformation, and the development of this stress boundary layer is shown by the curves labeled $\Lambda_0 = 1/3$ in Fig. 17(a). The results in Fig. 17 show that development of this elastic stress boundary layer depends on the initial aspect ratio and can be eliminated by using larger Λ_0 in the design. This is because larger initial aspect ratios provide more homogeneous kinematics in the liquid at short times, and consequently a more uniform deformation history at small strains. For the viscoelastic liquid, a more homogeneous deformation history at short times will in turn have a dramatic impact on the polymer stress growth and spatial distribution at all later times. The effects of the initial aspect ratio on the stress distribution along the centerline are shown in Fig. 17(b) at a high strain level of $\varepsilon = 3.8$. It can be seen that the extensional stress at large strains becomes more

uniform with larger Λ_0. The above arguments also apply to the shear stress component τ_{rz}. The only major difference is that the shear stress is anti-symmetric with respect to the mid-plane while the extensional stress is symmetric. Consequently, the location of the shear stress concentration is different from the extensional stress. For shear stress, the thin surface boundary layers are developed at two symmetric locations about the mid-point of the free surface as shown in Fig. 16, with one being above the mid-point of the free surface (the red-colored area) and the other below the mid-point of the free surface (the grey-colored area). The numerical results show that there is a correlation between stress concentration and curvature of the free surface. The high concentration of the tensile stress occurs near the region of minimum axial curvature, while the shear stress is concentrated in the region of maximum (or rapidly changing) free surface curvature.

Due to the stress growth, the polymer contribution becomes much larger than the viscous stress at large strains as indicated by the curves for $\varepsilon = 3.8$ in Fig. 18, in which a second stress boundary layer is developed near the two end-plates. At the strain of $\varepsilon = 3.8$, the extensional strain rate becomes uniform in the central part as indicated by the slope of u_z curve in Fig. 9, while the extensional stress remains axially non-uniform. Therefore, the numerical results suggest that homogeneity of stress is far more difficult to achieve than the homogeneity of strain rate because of the integrated effects of the deformation history on the resulting polymer stress. Small initial aspect ratios result in significant deviations from the ideal flow kinematics at the inception of motion and hence introduce a non-ideal deformation history for small strains. Although the flow kinematics can always approach the ideal homogeneous limit at large strains, the stress distribution may still be far from homogeneous due to the non-homogeneous deformation history the fluid elements experience at small strains.
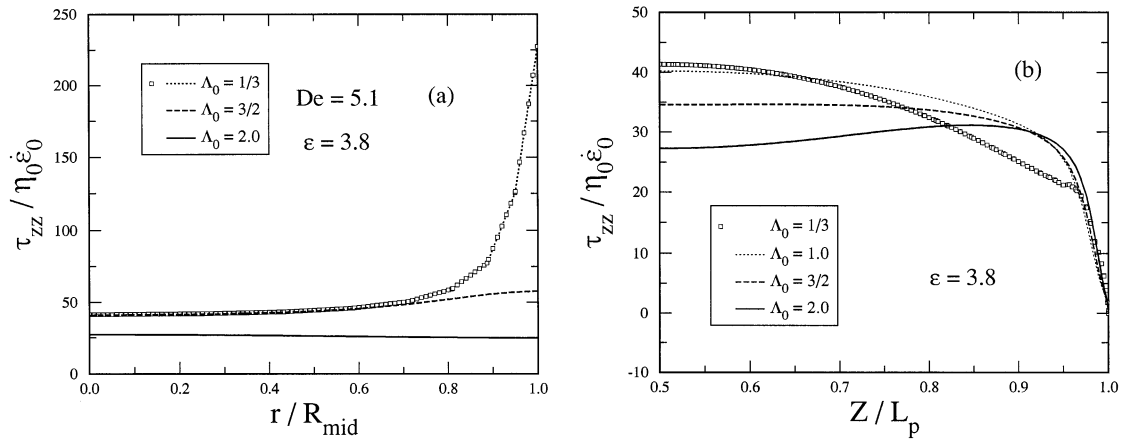

Fig. 17. The effects of the initial aspect ratio on the radial and axial stress distribution. (a) Radial variations of the total extra stress component, τ_{zz}, along the mid-point radius; (b) axial variations of τ_{zz} along the centerline of the liquid bridge ($r = 0$, only half of the axial filament length is shown here).
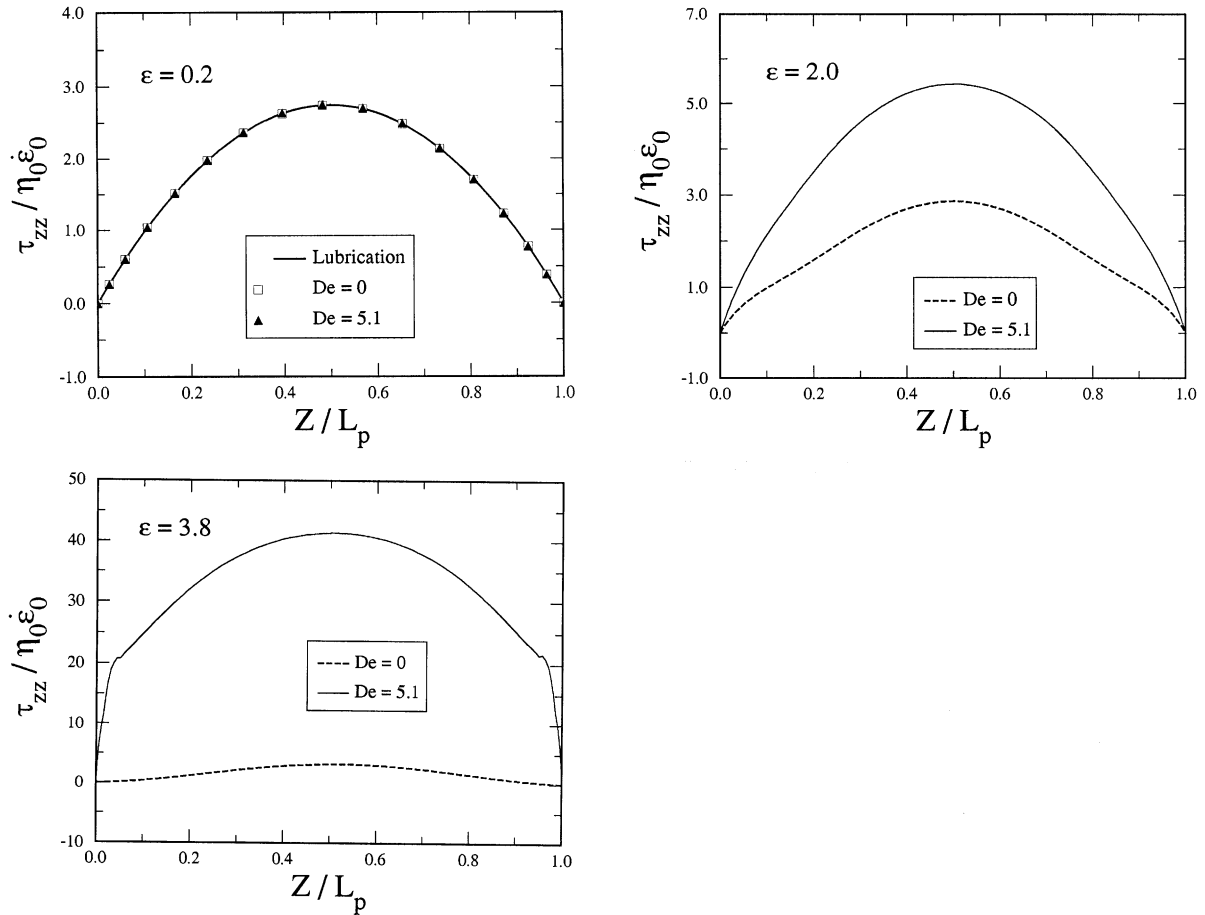
Fig. 18. Variation of the total extra stress component, τ_{zz}, along the centerline ($r = 0$) of the liquid bridge at three typical strain levels. Viscoelastic liquid (with Deborah number De = 5.08) vs. Newtonian liquid (De = 0). The solid curve denoted by 'lubrication' in (a) is based on the lubrication solution for Newtonian fluid, Eq. (28).

4.6. Transient extensional viscosity

We have shown that in filament stretching devices the flow kinematics are modified by the pinning conditions at the end-plates and the resulting extensional deformation is non-homogeneous. As a result, the predicted Trouton ratio based on the measured axial force F_z exerted on the end-plate deviates from the classical result for the initial stage when Hencky strain is small, as shown in Figs. 19 and 20. In Fig. 19 we compute the non-dimensional average normal stress $F_z^* = F_z/(\pi R_0^2 \eta_0 \dot{\varepsilon}_0)$ at the end-plate and plot it as a function of Hencky strain for three different initial aspect ratios. Computation of an extensional viscosity or Trouton ratio for both Newtonian and viscoelastic fluids will therefore deviate from the result expected in an ideal uniaxial elongational flow. The error depends on the initial aspect ratio and can be reduced by using larger values of Λ_0.
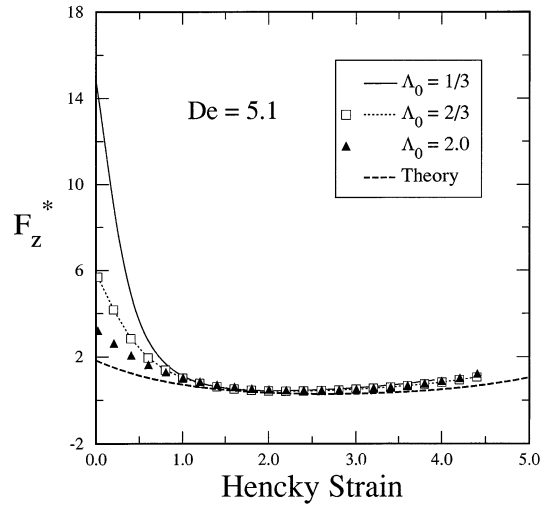
Fig. 19. Effects of the initial aspect ratio on the axial normal force defined in Eq. (24) at the moving end-plate. The dimensionless F_z^* is scaled by $F_z^* = F_z/(\pi R_0^2 \eta_0 \dot{\varepsilon}_0)$ and is equivalent to the average normal stress exerted on the end-plate. The numerical results are based on the half-length model. The 'Theory' curve is based on the homogeneous stress τ_{zz} in the transient start-up of uniaxial elongational flow.

For a Newtonian liquid, the lubrication solution and asymptotic analysis suggest that the initial deviation in Tr is proportional to Λ_0^{-2} and decreases with the increase of strain [9],
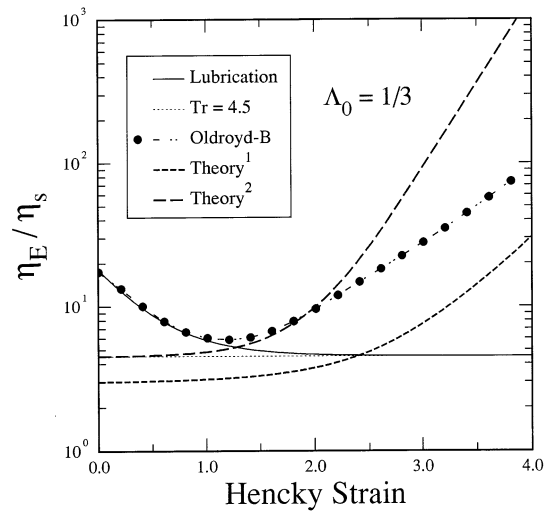

Fig. 20. Comparison of numerical predictions of the transient Trouton ratio with theory. The curve denoted by 'Oldroyd-B' is obtained from numerical simulation and calculated using the imposed $\dot{\varepsilon}_0$ in Eq. (23). Theory[1] and Theory[2] are obtained using $\dot{\varepsilon}_0$ and $1.5\dot{\varepsilon}_0$ in Eq. (25), respectively. The lubrication solution is based on Eq. (36).
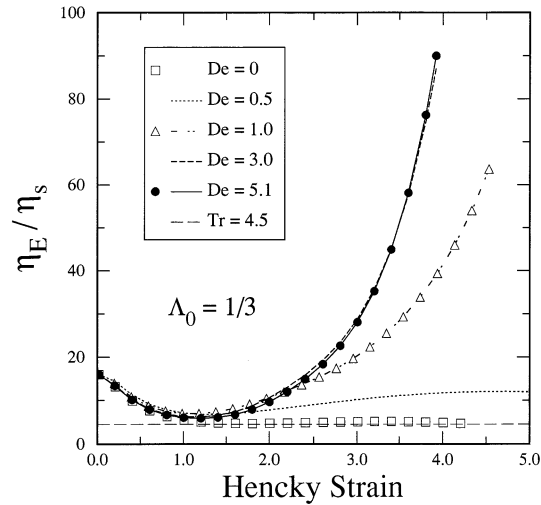
Fig. 21. Comparison of the transient Trouton ratio for the PIB test fluid given in Table 1 at five different Deborah numbers and with a small initial aspect ratio $\Lambda_0 = 1/3$. De = 0 corresponds to the Newtonian fluid. The results are based on simulations with the half-length model. Here η_E is scaled by the solvent viscosity η_s in order to compare with the Newtonian case.

approximately as

$$ \text{Tr} \approx \frac{3}{2}\left(3 + \frac{1}{\Lambda_0^2} e^{-7/2\dot{\varepsilon}_0 t}\right). \tag{36} $$

This variation in Tr with strain is shown in Fig. 20 by the solid line. Since the local extensional strain rate at the mid-plane is always approximately 1.5 times of the imposed extension rate (cf. Figs. 13 and 14), the curve asymptotes to $1.5 \times 3 = 4.5$ at large strains if the imposed extension rate $\dot{\varepsilon}_0$ is used in Eq. (23). Another way to interpret the definition of Tr is to use the effective extension rate at the mid-plane, i.e. $\dot{\varepsilon}_{\text{eff}} = 1.5\dot{\varepsilon}_0$ in Eq. (23). This will lead to the expected classical result of Tr = 3 for a Newtonian liquid at large strains.

For the Oldroyd-B liquid shown in Fig. 20, the calculated variation in Tr is almost identical to the Newtonian result given in Eq. (36) within the small strain range $\varepsilon < 1$. The short dash curve denoted by 'Theory[1]' in Fig. 20 is based on the theoretical result Eq. (25) for the start-up uniaxial elongational flow with an imposed extension rate $\dot{\varepsilon}_0$ and serves as a lower bound of the predicted Trouton ratio. If perfect uniaxial elongational kinematics were achieved in the liquid bridge at all times, the numerically computed Tr should be identical to this curve. However, a significant deviation between the Oldroyd-B computation and this curve can be seen in Fig. 20 for both the small and large strain ranges. The error in the small strain range is mainly due to the small initial aspect ratio, $\Lambda_0 = 1/3$ in this case. The error at large strain levels is caused by the non-ideal deformation history the liquid particles at the mid-plane experienced during the initial small strain stage. The curve labeled as 'Theory[2]' in Fig. 20 is based on the local extensional strain rate at the mid-plane, i.e. $\dot{\varepsilon}_{\text{eff}} \approx 1.5\dot{\varepsilon}_0$ and hence can be considered as an upper bound of the numerical prediction.

A comparison of the predicted transient extensional viscosity for five selected Deborah numbers is given in Fig. 21. The same small initial aspect ratio $\Lambda_0 = 1/3$ is used in all the cases.

De = 0 corresponds to the Newtonian fluid with the same solvent viscosity. In this case the curve labeled calculations approach Tr ≈ 4.5 as predicted by the lubrication and asymptotic solution in Eq. (36). Within the small strain range $0 \leq \varepsilon < 1.5$, the extensional behaviors at the various Deborah numbers are very similar as can be seen in Fig. 21. This suggests that the initial fluid response in the filament stretching devices is dominated by the non-homogeneous flow kinematics and deformation history arising from the small initial aspect ratio. At large strains, the extensional viscosity increases dramatically at higher Deborah numbers. For the range of computations shown, the curves at De = 3.0 and De = 5.1 also superpose when plotted as function of Hencky strain, in good agreement with experimental observations [4,9].

5. The reducing diameter device

As we have seen from the numerical results presented in the previous section, the kinematics attained in the conventional filament stretching devices deviate from ideal uniaxial elongational flow and the actual extensional deformation is non-homogeneous. The flow non-homogeneity is especially bad for small initial aspect ratios and small strains. This non-ideal kinematic history during the initial deformation of the filament will in turn have a direct impact on the evolution of the polymeric stresses. As a result, significant errors may be introduced in the predicted material properties of a fluid. Perhaps the simplest theoretical solution for the problem is to use larger initial aspect ratios in the design as evidenced by the numerical results in Section 4. However, in reality larger values of Λ_0 are impractical due to gravitational body forces which can cause the liquid bridge to sag or collapse [18] unless microgravity conditions can be achieved. Furthermore, larger values of Λ_0 require much longer final lengths in the stretching devices which can be difficult and expensive to accomplish in the design.

An alternative approach to improving the flow kinematics at short times is to introduce a so-called reducing diameter device (RDD) into the design. In an RDD, the diameter of the end-plate is no longer fixed, but instead is reduced at an exponential rate as the sample is elongated. It is hoped that this adaptive boundary condition at the end-plates will lead to improved flow kinematics at short times and hence better measurements of extensional material properties [6].

In this section, we examine the benefits of adaptive diameter end-plates in minimizing non-homogeneous kinematics within the fluid column. One important design parameter that deserves special consideration is the RDD ratio defined as

$$R_{\mathrm{D}} \equiv R_0/R_{\mathrm{stop}} \geq 1, \tag{37}$$

where R_{stop} is the radius at which the RDD stops contracting. This is not necessarily the end of the stretching process, however, since the elongation may still continue after the RDD stops. $R_{\mathrm{D}} = 1$ corresponds to fixed diameter end-plates. Theoretically, we would like R_{D} to be unbounded so that homogeneous kinematics can be achieved throughout the test. In practice, however, the achievable range of R_{D} is restricted by mechanical design considerations. To relate R_{D} to the global Hencky strain, we rewrite Eq. (37) using Eq. (27) in the following forms

$$R_{\mathrm{D}} = \mathrm{e}^{0.5\varepsilon_{\mathrm{f}}} \quad \text{or} \quad \varepsilon_{\mathrm{f}} = 2 \ln R_{\mathrm{D}}. \tag{38}$$

For a given final Hencky strain ε_f, estimates of the required R_D value can be easily obtained via Eq. (38). For instance, in order to attain $\varepsilon_f = 5$, a 12:1 R_D is required. This would appear to be extremely difficult to accomplish via mechanical design. Berg and co-workers [6] constructed a device capable of attaining $R_D = 2$. Naturally, a question that needs to be answered is what benefits can be extracted from a RDD design with a limited value of R_D. Our studies of the deformation history in the filament stretching rheometer indicate that for viscoelastic fluids, the most significant non-homogeneous extensional deformation occurs primarily within a particular strain range of $0 < \varepsilon \leq 2$ and the deformation becomes increasingly uniform with strain hardening at $\varepsilon > 2$. This suggests that an RDD design with a limited R_D may still lead to a marked improvement in the flow kinematics. In particular, the minimum R_D that covers a working range of strains up to $\varepsilon = 2$ is found to be $R_D \approx 2.71$ based on Eq. (28), and an RDD ratio of 3:1 or greater is desirable.

In this work, we consider a postulated RDD design with $R_D = 4$. In this case, the global Hencky strain based on the axial displacement of the end-plates is about $\varepsilon \approx 2.77$ when the RDD stops contracting, which is well above the strain level for strain hardening to develop. In order to compare with the conventional filament stretching devices, three possible designs were considered:

1. 4:1 RDD at one (upper) end-plate (referred to below as 4:1 1-RDD),
2. 4:1 RDD at both end-plates (referred to below as 4:1 2-RDD),
3. Fixed diameter at both end-plates.

The following reducing diameter boundary condition is imposed at the RDD end-plate

$$\frac{R(t)}{R_0} = \begin{cases} e^{-0.5\dot{\varepsilon}_0 t} & \dot{\varepsilon}_0 t \leq 2.77, \\ 1/4 & \dot{\varepsilon}_0 t > 2.77. \end{cases} \tag{39}$$

A comparison of the simulated free surface shapes is presented in Fig. 22. Unsurprisingly, the 4:1 2-RDD design appears to be able to provide the most uniform extensional deformations among the three design tests. The results show that for the 4:1 2-RDD design the liquid bridge retains its cylindrical shape before the RDD stops. After the RDD stops at $\varepsilon = 2.77$, the aspect ratio has become so large that the free surface shows only a very slight deflection at $\varepsilon = 3.1$ and remains axially uniform over most of the liquid bridge at all higher strains.

For an RDD device capable of a limited value of R_D, a major concern is how the non-homogeneity evolves after the RDD stops contracting and what type of error control criteria could be used to ensure satisfactory homogeneity in the kinematics. To address these issues we return to the concept of a homogeneous deformation zone (HDZ) introduced in Section 4.3. One important objective of the RDD design is to create a HDZ within which the desired flow kinematics can be achieved at all times during the stretching process, especially after the RDD stops. It is evident that after the RDD ceases to contract radially, the no-slip boundary condition at either end-plate will induce kinematic non-homogeneities; however, the volume of liquid affected will be small. For the purposes of preliminary design calculations such as those presented here, we characterize the uniformity of the HDZ by the temporal and spatial homogeneity of the axial velocity gradient $D_{zz}(r, z, t)$, and indicate $\pm 10\%$ ranges of the relative error with respect to the imposed extension rate $\dot{\varepsilon}_0$ in Figs. 23 and 24.

The temporal homogeneity condition characterized by $\dot{\varepsilon}_{eff}$ (Eq. (35)) controls the history of the local extensional strain rate at the R_{min} plane. A typical comparison of the evolution in $\dot{\varepsilon}_{eff}$ for

the three different rheometer end-plate designs is shown in Fig. 23. Although the presence of an RDD at one end-plate provides some improvement in temporal homogeneity over the fixed diameter design, the variations are still much larger than 10%. The design with 4:1 RDDs at
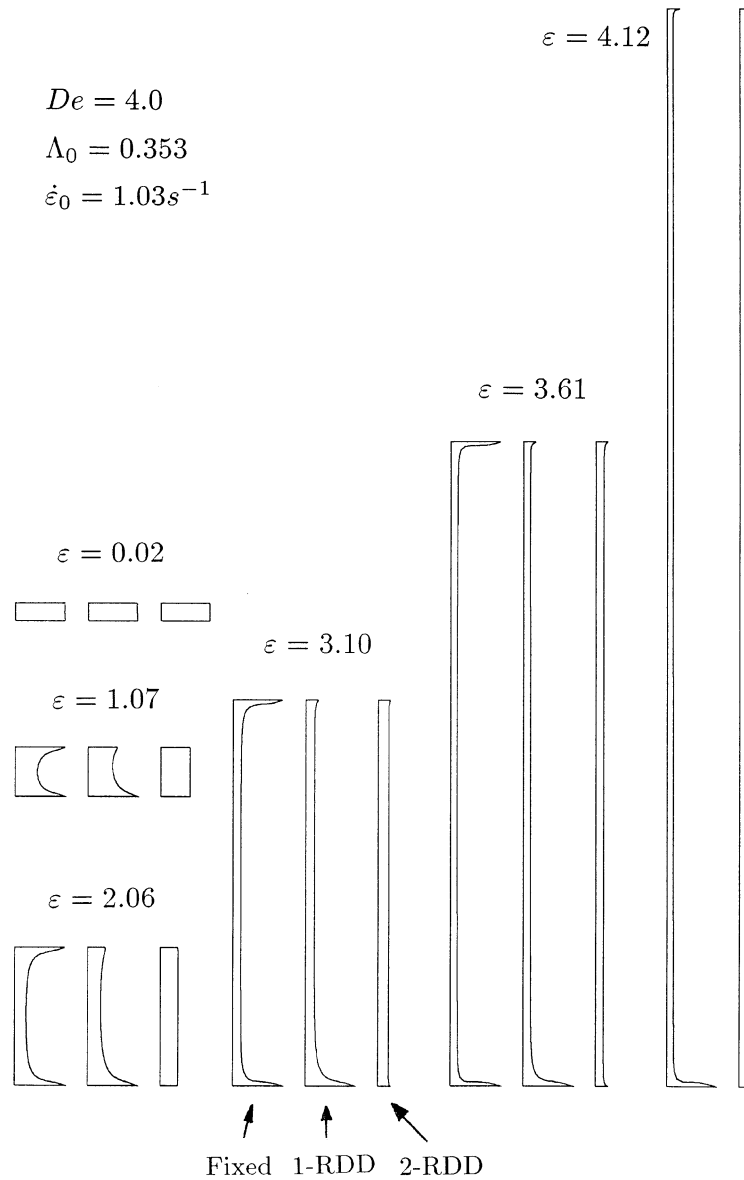
$$\varepsilon = 4.12$$

$$De = 4.0$$
$$\Lambda_0 = 0.353$$
$$\dot{\varepsilon}_0 = 1.03 s^{-1}$$

$$\varepsilon = 3.61$$

$$\varepsilon = 0.02$$

$$\varepsilon = 3.10$$

$$\varepsilon = 1.07$$

$$\varepsilon = 2.06$$

Fixed 1-RDD 2-RDD

Fig. 22. Comparison of the simulated free surface shapes at six selected Hencky strain levels for the three possible rheometer designs. The fluid used in the modeling is a polystyrene-based Boger fluid (PS) and the geometry and its material properties are listed in Table 1. The 4:1 RDD is stopped at $\varepsilon = 2.77$. For the 1-RDD test, the upper boundary represents the RDD end-plate. Only the right half-plane of the axisymmetric fluid filament is shown.
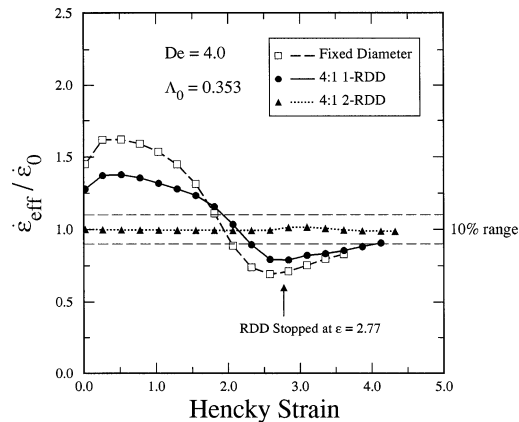
Fig. 23. A quantitative comparison of the variation in the local extensional strain rate at the mid-plane between two end-plates for the simulated design tests. Here the temporal homogeneity of the extensional deformation is characterized by the effective extension rate $\dot{\varepsilon}_{eff}$ and calculated based on Eq. (35).

both end-plates provides perfect temporal homogeneity for $\varepsilon < 2.77$ and the deviations remain very small even after the RDD stops.

Spatial homogeneity in D_{zz} requires that at any given time, the axial variation of D_{zz} should be within, say, $\pm 10\%$ of the imposed extension rate throughout the HDZ. Detailed examination of the axial variations in the extensional velocity gradient D_{zz} along the centerline of the liquid bridge are presented in Fig. 24 for increasing levels of Hencky strain. For the fixed end-plate design, a spatially homogeneous strain rate is only achieved at very large strains ($\varepsilon > 5$). Spatial variations in the 1-RDD design also exceed the desired 10% range for $\varepsilon < 4$. Another drawback of the 1-RDD design is that it does not preserve the axial symmetry about the mid-plane and the position of minimum radius shifts during the course of the experiment. With RDDs at both end-plates, the value of D_{zz} is identical to that in the ideal uniaxial elongational flow until the RDDs stop contracting. At high strains, it can be seen from Fig. 24 that steep boundary layers in the velocity gradient develop near the two end-plates due to the changed boundary conditions and these regions make numerical calculations difficult. However, the relative error in the spatial variation of D_{zz} remains small throughout the central region of the column.

In addition to spatial homogeneity in the axial deformation, to achieve a uniaxial extensional flow it is also necessary to eliminate the undesired shear deformation by reducing the shear rate $D_{rz}(r, z, t)$ to be less than some percentage of $\dot{\varepsilon}_0$. Variations in the shear velocity gradient on the free surface of the deforming filament are shown in Fig. 25 together with $\pm 20\%$ error bounds for illustration. It can be seen that fixed diameter end-plates result in significant shear rates for strains up to $\varepsilon \sim 3$. The 1-RDD design cannot achieve a shear free deformation condition for the strain range $\varepsilon < 4.12$. By contrast, incorporating an RDD at each end of the rheometer can successfully eliminate shear near the end-plates and also along the free surface leading to a nearly ideal shear-free deformation history. Finally, we compare in Fig. 26 the predicted transient Trouton ratios for the three postulated rheometer designs. Among the three configurations considered, the 4:1 2-RDD design provides the most accurate prediction of Tr. The results
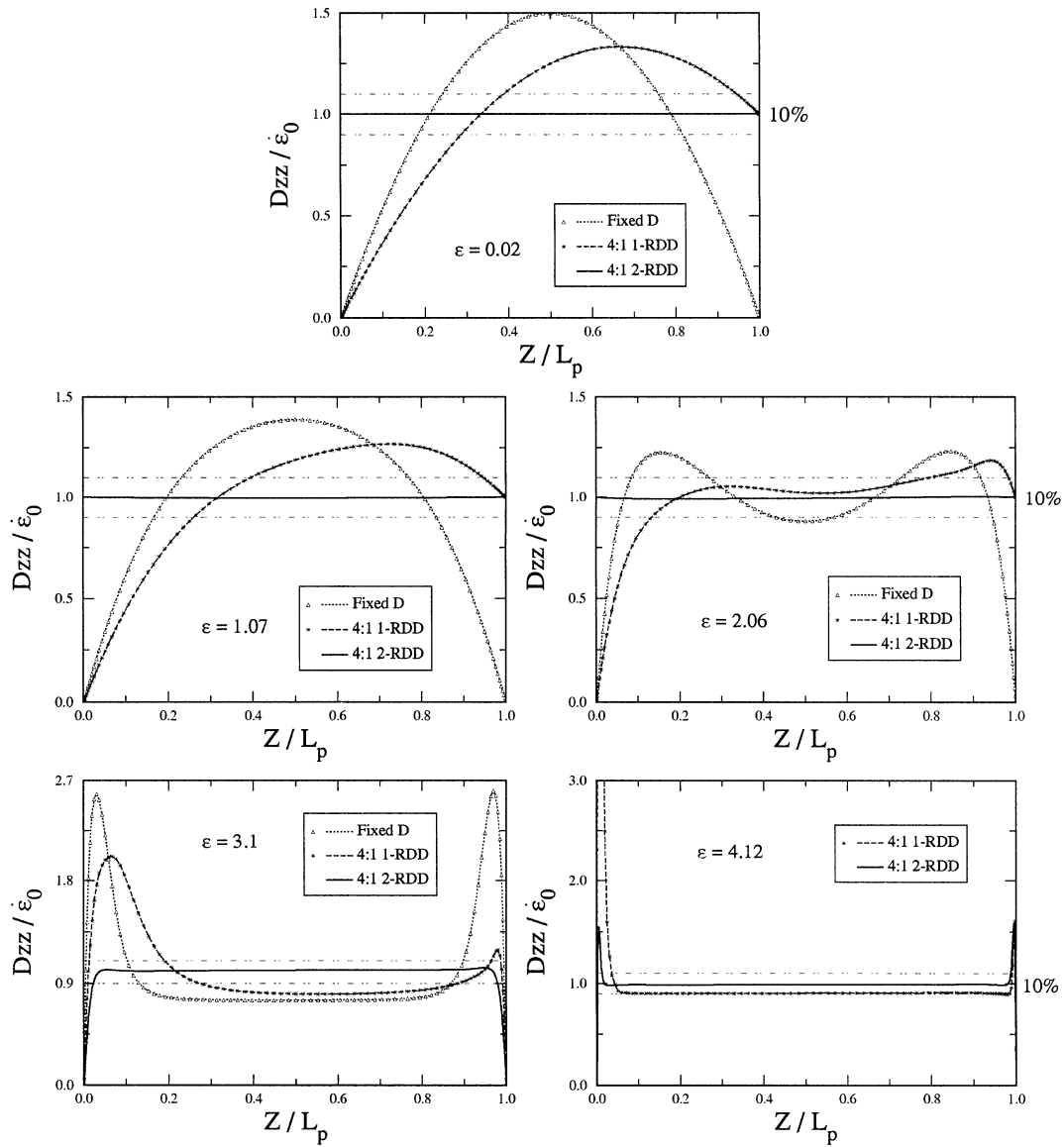
Fig. 24. Axial variation of the extensional velocity gradient D_{zz} along the centerline $r = 0$ for the design tests with $\Lambda_0 = 0.353$, De $= 4.0$. A numerical check for the spatial homogeneity of the extensional deformations created in the three experimental designs of the filament stretching devices.
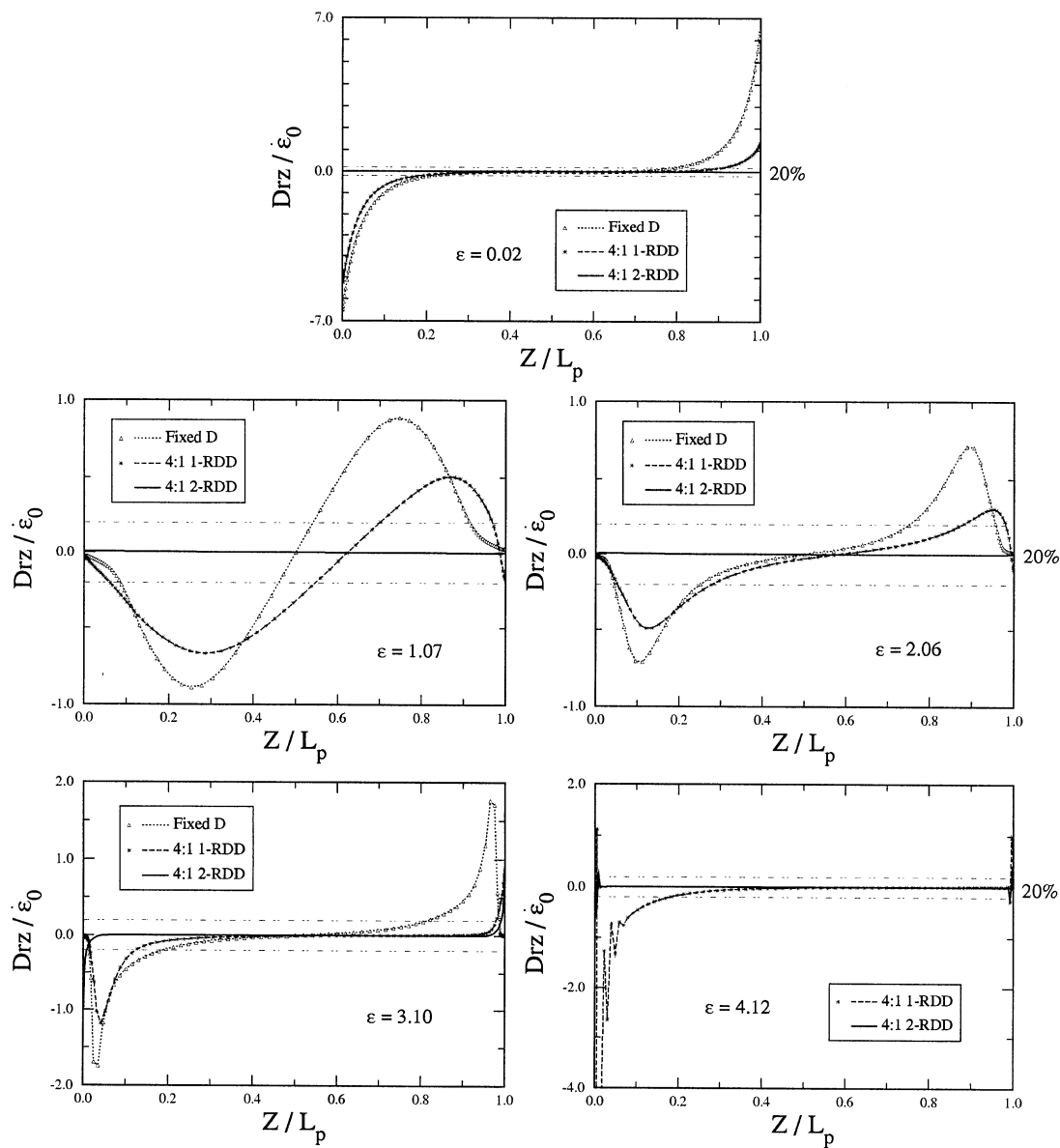
Fig. 25. Variation of the shear velocity gradient D_{rz} on the free surface for the design tests with $\Lambda_0 = 0.353$, De $= 4.0$. Incorporating RDD at both end-plates effectively eliminates non-homogeneous shear flow near the end-plates and along the free surface.

shown in Fig. 26 suggest that while a single RDD offers only slight improvement, the 2-RDD case can provide accurate agreement with theory.

6. Conclusions

We have presented numerical calculations of the fluid kinematics and the dynamic evolution in the viscoelastic stresses for a filament stretching rheometer. For Newtonian fluids and small initial aspect ratios, the flow kinematics in the liquid bridge at small strains can be accurately approximated by a lubrication solution [9]. Although the simple lubrication solution Eq. (28) is derived for Newtonian fluids, comparisons with full-scale numerical solutions show that it is also a good approximation at small strains for liquid bridges with a large solvent viscosity that can be modeled by the Oldroyd-B constitutive equation. This conclusion is in agreement with the experimental and computational work on the squeeze flow problem by Phan-Thien and Boger [24,25]; it also agrees well with the experimental observations of Spiegelberg et al. [9] in a filament stretching device. Both the lubrication solution and the full-scale numerical solution presented in this work show that for typical experimental conditions, the fluid deformation generated in the liquid bridge is spatially and temporally inhomogeneous and an analysis based on the net tensile force measurements does not lead to true extensional material properties.

We have shown through the numerical simulations that the dynamical behavior of viscoelastic fluids is dramatically different from Newtonian liquids. At Deborah numbers De > 0.5, strain hardening occurs beyond $\varepsilon = 2$ and is manifested globally as a change in the slope of the mid-point radius versus time, and a rapid increase in the tensile stress in the filament. This predicted strain-hardening phenomenon is in a good agreement with the available experimental
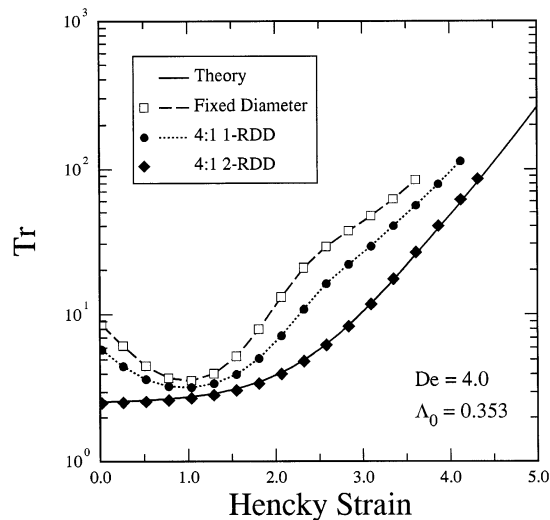
Fig. 26. Comparison of the predicted transient Trouton ratio with theory for the design tests. The 4:1 2-RDD design provides the most accurate prediction of Tr among the three test cases.

measurements [2,3,7,9] and, in contrast to the evolution of a Newtonian filament, results in the formation of an increasingly uniform cylindrical viscoelastic filament. The predicted break-up mechanism in viscoelastic liquid bridge at high De is also quite different from the Newtonian case. For Newtonian fluids, there is no strain-hardening and 'necking' always decreases the filament radius fastest at the fluid mid-plane between the two end-plates. Consequently, Newtonian liquid bridges in filament stretching devices will break in the middle. For viscoelastic fluids, the strain hardening at large Hencky strains inhibits the filament from breaking in the middle. Instead, the rapid amplification of liquid drainage from the end-plate regions will ultimately initiate the onset of an elastic instability in the vicinity of the end-plates. Our numerical calculations of the evolution of the free surface agree well with the experimental observations reported in [10] and also with those simulated by Sizaire and Legat using the FENE-CR model [29]. Indeed for the range of strains ($\varepsilon \leq 4$) covered in [29] and the present work, the filament shapes predicted by the FENE-CR and Oldroyd-B models are practically indistinguishable. The progressive drainage of the quasi-static fluid reservoirs present at each rigid end-plate provides a rationalization for the elastic instability and decohesion phenomena observed experimentally at large Hencky strains.

As a result of the spatially inhomogeneous deformation at short times, the development of a stress localization or 'boundary layer' in the polymer stress near the free surface is observed. In experiments, such radial stress distributions within the liquid filament are almost impossible to measure, and force measurements are interpreted as resulting from a radially uniform fluid stress. The numerical results predict an important difference in the stress behavior between the viscoelastic and the Newtonian liquids. For Newtonian filaments, the local stress concentration in the vicinity of the mid-point of the free surface is present only at small strains and eventually decays at larger strain levels as the extension rate D_{zz} becomes radially uniform across the mid-plane. For the Oldroyd-B fluid with a small initial aspect ratio, the local stress inhomogeneity evolves with the strain throughout the deformation history and leads to the formation of a thin stress boundary layer at larger strains even when a homogeneous extensional strain rate is reached. This stress boundary layer development is a direct consequence of the elastic properties of the material, as the viscoelastic liquid 'remembers' the non-homogeneous deformation and pre-shearing history it experienced at small strains. Design calculations for different aspect ratios suggest that the development of the stress boundary layer depends on the initial aspect ratio and can be eliminated by using larger initial aspect ratios in the design.

Our numerical observations of the stress concentration and boundary layer development agree qualitatively well with the results of the configuration tensor $A \equiv \langle QQ \rangle / Q_{eq}^2$ given by Sizaire and Legat [29]. Here $\langle QQ \rangle$ represents an ensemble average over the configuration space of the dyadic product, QQ, of the dumbbell end-to-end vector Q, and Q_{eq}^2 is the mean square end-to-end distance between the two beads. The radial variation of the extensional component of the configuration tensor in Fig. 5 of Ref. [29] shows a non-homogeneous extensional deformation at the macromolecular level on the mid-point plane. The macromolecules, represented by elastic dumbbells in the kinetic theory, are more elongated near the curved free surface than in the central region of the liquid filament. For small initial aspect ratios, this non-homogeneous microscopic extensional deformation leads to the macroscopic localization of the liquid extension rate and the development of a stress boundary layer observed in the present work.

The most effective approach to improving the homogeneity of the flow kinematics at short times is to simultaneously elongate the sample axially and reduce the diameter of the end-plate fixtures at an exponential rate. One inherent physical limit with such reducing diameter device is that the radial engineering strain attainable, defined by the RDD ratio in Eq. (37), is usually restricted by the mechanical design of the instrument to be much lower than the total axial strain of the experiment. Analysis indicates that an RDD rate of 3:1 or greater is necessary to preserve homogeneous extensional deformation up to the onset of pronounced strain hardening. Comparisons based on three postulated designs show that introduction of 4:1 RDDs at both end-plates is good enough for providing a nearly ideal shear-free deformation history and greatly enhances accuracy in the measurements than with conventional filament stretching devices using fixed diameter end-plates. Of course, in the current experimental realizations of such devices, an alternate approach has been to adjust the end-plate boundary data for $\dot{L}_p(t)$ to result in exponential decrease in $R_{mid}(t)$ at all times. While such an approach leads to a temporal homogeneity in $\dot{\varepsilon}_{eff}(t)$, the fluid deformation remains spatially inhomogeneous. As a result, selection of the 'correct' or optimum profile for $\dot{L}_p(t)$ must be adjusted ad hoc on a fluid-by-fluid and rate-by-rate basis. Now that we have developed a fundamental and systematic understanding of the evolution in the shape and kinematics of viscoelastic fluid columns in a filament stretching rheometer, it will be possible to investigate this more complex boundary motion in detail, and provide heuristic guidelines for optimizing experimental test protocols.

Acknowledgements

References

[1] M.M. Denn, in: J.L. Lumley, A. Acrivos, L.G. Leal, S. Leibovich (Eds.), Research Trends in Fluid Dynamics, AIP Press, Woodbury, New York, 1996, p. 69.
[2] D.F. James, K. Walters, in: A.A. Collyer (Ed.), Techniques in Rheological Measurement, Chapman and Hall, London, 1993, Ch. 2.
[3] T. Sridhar, V. Tirtaatmadja, D.A. Nguyen, R.K. Gupta, J. Non-Newtonian Fluid Mech. 40 (1991) 271.
[4] V. Tirtaatmadja, T. Sridhar, J. Rheol. 37 (1993) 1081.
[5] R. Kröger, S. Berg, A. Delgado, H.J. Rath, J. Non-Newtonian Fluid Mech. 45 (1992) 385.
[6] S. Berg, R. Kröger, H.J. Rath, J. Non-Newtonian Fluid Mech. 55 (1994) 307.
[7] M.J. Solomon, S.J. Muller, J. Rheol. 40 (1996) 837.
[8] S. Gaudet, G.H. McKinley, H.A. Stone, Phys. Fluids 8 (1996) 2568.
[9] S.H. Spiegelberg, D.C. Ables, G.H. McKinley, J. Non-Newtonian Fluid Mech. 64 (1996) 229.
[10] S.H. Spiegelberg, G.H. McKinley, J. Non-Newtonian Fluid Mech. 67 (1996) 49.
[11] R.B. Bird, R.C. Armstrong, O. Hassager, Dynamics of Polymeric Liquids, Vol. 1, Fluid Mechanics, 2nd ed., Wiley, New York, 1987.

[12] V. Tirtaatmadja, T. Sridhar, J. Rheol. 39 (1995) 1133.
[13] D.F. James, T. Sridhar, J. Rheol. 39 (1995) 713.
[14] P.R. Schunk, J.M. de Santos, L.E. Scriven, J. Rheol. 34 (1990) 387.
[15] J. Sun, N. Phan-Thien, R.I. Tanner, J. Non-Newtonian Fluid Mech. 58 (1995) 219.
[16] R.W.G. Shipman, M.M. Denn, R. Keunings, J. Non-Newtonian Fluid Mech. 40 (1991) 281.
[17] J.G. Oldroyd, Proc. R. Soc. A200 (1950) 523.
[18] L.A. Slobozhanin, J.M. Perales, Phys. Fluids A5 (1993) 1305.
[19] M. Yao, G.H. McKinley, (1996) (in preparation).
[20] Polyflow User's Manual, ver. 3.4.0., Polyflow s.a., Place de l'Université 16, B-1348, Louvain-la-Neuve, Belgium, 1995.
[21] J.F. Thompson, Z.U.A. Warsi, C. Wayne Mastin, Numerical Grid Generation—Foundations and Applications, Elsevier, Amsterdam, 1985.
[22] R.D. Gillette, D.C. Dyson, Chem. Eng. J. 2 (1971) 44.
[23] J. Stefan, Sitzungber, K. Akad. Wiss. Math. Natur. Wien 69 (1874) 713.
[24] N. Phan-Thien, R.I. Tanner, J. Non-Newtonian Fluid Mech. 14 (1984) 327.
[25] N. Phan-Thien, J. Dudek, D.V. Boger, V. Tirtaatmadja, J. Non-Newtonian Fluid Mech. 18 (1985) 227.
[26] H.C. Lee, IBM J. Res. Dev. 18 (1974) 364.
[27] J. Meseguer, J. Fluid Mech. 130 (1983) 123.
[28] S.L. Goren, M. Gottlieb, J. Fluid Mech. 120 (1982) 245.
[29] R. Sizaire, V. Legat, J. Non-Newtonian Fluid Mech. 71 (1997) 89–108.